AN ABSTRACT OF THE THESIS OF

Wenrui Zhao for the degree of Master of Science in Materials Science presented on December 4, 2020

Title: Significance of Grain Refinement on High Entropy Alloys Processed through High-Pressure Torsion

Abstract approved:

_____

Megumi Kawasaki

High entropy alloys (HEAs) are well known for their excellent mechanical properties compared to conventional metallic alloys. The application of High-Pressure Torsion (HPT) processing reduces grain size of materials away below 1 μm. This significant grain refinement leads to an improvement in mechanical properties, such as strength and ductility. In the present study, HPT processing is applied on three different HEAs, as-cast CoCrFeNi, 3D-printed CoCrFeNi, and as-cast HfNbTiZr, under a compressive pressure of 6 GPa at a rotation speed of 1 rpm for up to 8 turns at room temperature. Hardness measurements demonstrate the significant hardness increase towards homogeneously distributed high hardness within the HEAs. The X-ray diffraction analysis demonstrates the structural evolution including texture and crystallite size changes in the HEAs during grain refinement, and additional support for microstructural changes are shown in SEM and TEM images. Nanoindentation is applied to examine the micro-mechanical properties of the HEAs and an improvement in plasticity is shown by an increase in strain rate sensitivity in the

HPT-processed HEAs. This study demonstrates the feasibility of improving the mechanical properties of HEAs through HPT processing.

Significance of Grain Refinement on High Entropy Alloys Processed through High-Pressure Torsion

by
Wenrui Zhao

A THESIS

submitted to

Oregon State University

in partial fulfillment of
the requirements for the
degree of

Master of Science

Presented December 4, 2020
Commencement June 2021

Master of Science thesis of Wenrui Zhao presented on December 4, 2020

APPROVED:

Major Professor, representing Materials Science

Associate Dean for Graduate Programs, College of Engineering

Dean of the Graduate School

I understand that my thesis will become part of the permanent collection of Oregon State University libraries. My signature below authorizes release of my thesis to any reader upon request.

Wenrui Zhao, Author

ACKNOWLEDGEMENTS

I would like to express my sincere appreciation to my advisor, Dr. Megumi Kawasaki for her support and encouragement throughout the writing.

TABLE OF CONTENTS

Page

TABLE OF CONTENTS (Continued)

Page

LIST OF FIGURES

Figure Page

LIST OF FIGURES (Continued)

Figure Page

LIST OF FIGURES (Continued)

Figure Page

LIST OF TABLES

Table Page

1 Introduction

Advancements in engineering materials and their mechanical properties are always desired in current manufacturing processing. However, since conventional metallic alloys are usually based on one primary element, there is a limitation for tailoring the compositions that fail to meet desired mechanical properties. The necessity of the new metallic materials introduced the concept of multi-principal element alloys, including high entropy alloys (HEAs), which are designed with three or more principal elements in equimolar or near equimolar, which have excellent and controllable mechanical properties with excellent structural stability at a wide range of temperatures. Among various HEAs, two specific elemental combinations of CoCrFeNi and HfNbTiZr are widely used and studied in the last decade. A CoCrFeNi alloy is the most common base HEA having an f.c.c. crystal structure developed for designing physical and mechanical properties by further adding some elements, and an HfNbTiZr alloy is a base HEA having a b.c.c. structure studied for developing the novel refractory materials.

Although the development in the manufacturing of HEAs moves forward, additional post-manufacturing processing can be another approach to improve mechanical properties. It is well known that, according to the Hall-Petch relationship, the yield strength of materials increases with reducing the grain size. Accordingly, grain refinement is considered an efficient approach to further improve mechanical properties. It is well accepted in the Materials Science community that the materials having grain sizes within a range of 100-1000 nm are called ultra-fine grained (UFG) materials. UFG materials show extraordinary mechanical properties in comparison with coarse-grained materials. Such UFG materials have an excellent potential of overcoming the strength-ductility paradox.

There are conventional and practical thermomechanical processing methods to achieve grain refinement in order to improve the mechanical properties of materials, such as cold/hot rolling, extrusion, and forging. However, these conventional processes often fail to reduce the grain size below 1 μm. Severe plastic deformation (SPD) is a well-recognized technique for introducing UFG materials having grain size below 1 μm, and the research field of SPD has been intensively studied for the last three decades. Among various developed SPD techniques, High-Pressure Torsion (HPT) is defined as one of the effective approaches to achieve real nanostructures for bulk samples by introducing a large amount of torsional strain under severe compression pressure.

In the present study, an HPT technique is applied to three different HEAs, as-cast CoCrFeNi HEA, 3D-printed CoCrFeNi HEA, and as-cast HfNbTiZr. These are processed for up to 8 turns under a compression pressure of 6 GPa at room temperature with a rotation speed of 1 rpm. By applying multiple characterization techniques, such as X-ray diffraction (XRD) line profile analysis, Vickers hardness measurements, nano-indentation hardness testing, and microstructural analyses through transmission electron microscopy (TEM) and scanning electron microscopy (SEM), this study evaluates and discusses the hardness evolution, microstructure changing, and plasticity changing. The emphasis is placed on the significant grain refinement and the unique mechanical response after HPT processing.

2 Literature Review

2.1 Ultrafine-Grained Materials

It is now well accepted that the materials having submicron grains from 100 to 1000 nm or nanocrystalline grains below 100 nm are defined as ultrafine-grained (UFG) materials [1]. Such fine grain sizes of UFG materials are defined as smaller than the current industrial thermo-mechanically processed fine-grained materials. Numerous studies show that grain size has a significant contribution to the mechanical properties of materials. In general, with decreasing grain size, materials show a large increase in strength and toughness [2], which is depicted in Figure 2.1.1 [3].

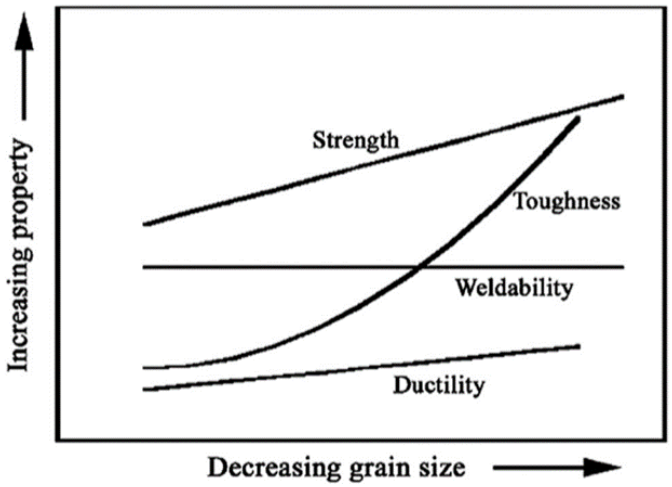

Figure 2.1.1 Mechanical properties vs grain size of metallic materials [3]

In practice, yield strength of crystalline materials is collated with grain size that is defined by the Hall-Petch relationship. The relationship description is given in the following form [4,5].

$$\sigma_y = \sigma_0 + k_y d^{-1/2} \quad (1)$$

where σ_0 is the lattice friction stress, k_y is the yielding constant. Thus, it indicates that the decrease in grain size leads to an increase in yield strength, and the trend of increasing strength with grain size reduction is well described in Fig. 2.1.1. On the contrary, small grain sizes often attribute to the loss of strain hardening and strain rate sensitivity leading to no improvement or even lowering in ductility of metals and alloys [6]. Thus, materials having ultrafine-grain sizes usually demonstrate high yield strength while they show low ductility, as described in Fig. 2.1.1. It should be noted that the line showing the ductility change with grain refinement in Figure 2.1.1. is arguable since ductility often goes down with grain refinement. However, in terms of UFG after SPD, often many UFG materials show improved strain rate sensitivity, thus plasticity, which gives a potential for the materials to demonstrate either the maintained or slightly improved ductility.

An inverse relationship of enhanced strength and reduced ductility is an inevitable issue for metal processing that introduces grain refinement, and it is called the paradox of strength and ductility, which is defined as “materials may be strong or ductile, but rarely both at once” [7], and is illustrated in Figure 2.1.2 [8]. Specifically, numbers of metals after cold-rolling are listed in the plot of yield strength vs. elongation to failure, and the shadow area describes the field where the materials within the region behave either ductile but not strong or strong, but brittle. The number of percentages indicates the volume reduction after rolling, thereby implies the original sample without rolling. This plot shows all listed metals before and after thermo-mechanical processing stay in the field under the shaded area, thereby demonstrating the paradox of strength and ductility of conventional materials [9].

However, two exceptions are shown in the plot where the nano Ti and nano Cu show both exceptionally high yield strength and excellent ductility and are placed in the white region

in the plot that is away from the earlier mentioned conventional materials. These nano Ti and nano Cu are processed by HPT [10] and ECAP [11], respectively, of severe plastic deformation (SPD) techniques, which will be discussed in the following section. In brief, metal processing by SPD techniques enable to introduce a large amount of the strain to materials, grain size will be refined below 1 μm, and the materials will have an opportunity to exhibit both high strength and ductility [12]. This indicates the special mechanical properties of UFG materials.

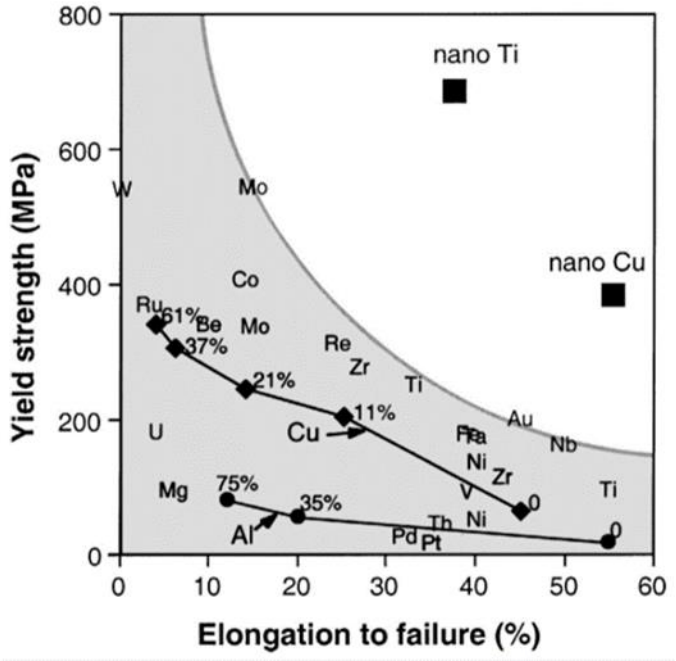

Figure 2.1.2 A plot of yield strength against elongation to failure [8]

Conventional thermo-mechanical processing involving grain refinement, such as cold/hot rolling, extrusion, and forging, generally fails to introduce UFG microstructure having grain sizes below 1 μm. Therefore, significant efforts have been placed in the last three decades on developing new processing techniques for introducing UFG metals and alloys [9].

2.2 Severe Plastic Deformation

Numerous SPD techniques are developed to produce UFG materials based on the work done by P.W. Bridgman about the application of the combination of high hydrostatic pressure and shear deformation during metal processing [7, 13]. SPD is defined as the metal forming methods, which can introduce a large amount of strain under high hydrostatic pressure and ultimately lead to exceptional grain refinement without having any significant change in the overall dimensions of samples [14]. Among the numerous reports of SPD techniques, Equal-channel angular pressing (ECAP), Accumulative roll bonding (ARB), Repetitive corrugation and straightening (RCS), and High-pressure torsion (HPT) are widely studied for the processing of UFG materials [15, 14].

Equal-channel angular pressing (ECAP) is one of the most developed SPD processing techniques, which is schematically shown in Figure 2.2.1 [14]. A sample in a billet shape is pressed by a solid die, which includes a bent channel having a consistent cross-sectional area. A simple shear strain is introduced in every single pass when the billet is pressed by a plunger and passes through the intersection of the bent part of the channel. Since the cross-sectional dimensions of the billet are kept unchanged, the sample can be processed repetitively to obtain exceptionally high accumulative strain [15]. The equivalent strain, ε_{eq}, introduced by ECAP is given the following equation [16],

$$\varepsilon_{eq} = \frac{N}{\sqrt{3}}\left[2\cot\left(\frac{\Phi}{2}+\frac{\Psi}{2}\right)+\Psi\operatorname{cosec}\left(\frac{\Phi}{2}+\frac{\Psi}{2}\right)\right] \quad (2)$$

where Ψ is the angle between two parts of the channel, Φ is the outer arc of the intersection, and *N* is the number of the ECAP passes.

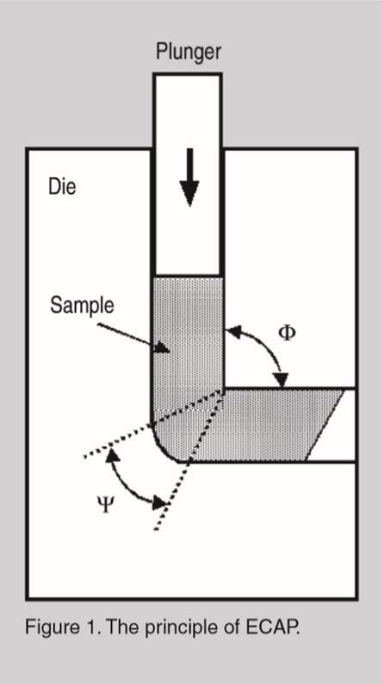

Figure 2.2.1 The principle of ECAP [14]

Even though the ECAP can produce the materials with excellent mechanical properties [17], the grain refinement efficiency of ECAP is still unsatisfactory, which requires many passes to reduce the grain size below 100nm [11].

Accumulative roll bonding (ARB) is a processing technique using conventional rolling facilities. The principles of ARB is shown in Figure 2.2.2 [18] where a sheet material is first rolled through the mill so that the thickness of the sheet material is reduced, the sheet is cut into two halves and stacked them together after some surface cleaning, and then the stacked sheet passes through the mill again and strained to have a lower thickness. By continuing the series of procedures, the sheet material receives a large amount of accumulated strain leading to UFG microstructure [14]. The effective equivalent strain of ARB process, ε_{eff}, is given by the equation below [18],

$$\varepsilon_{eff} = N\frac{2}{\sqrt{3}}\ln(\frac{t_0}{t}) \quad (3)$$

where N is the number of cycles, and t_0 and t are the thicknesses of the sample before and after ARB processing, respectively.

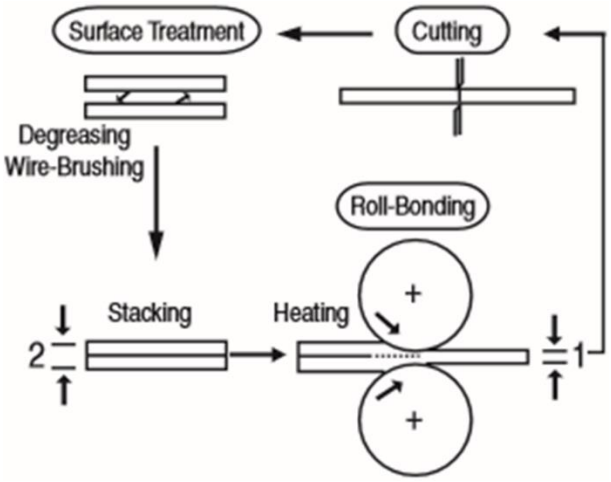

Figure 2.2.2 The principle of ARB [18]

The ARB process can be easily adapted in the current manufacturing technology. Nevertheless, the process is hard to form equiaxed ultrafine grains due to the nature of the technique, which introduces the asymmetric texture and microstructure, thus mechanical properties [19].

Repetitive corrugation and straightening (RCS) is a technique which can be applied to large-scale industrial production. The schematic view is shown in Figure 2.2.3 [20]. Specifically, the material in the shapes of plate or wire is deformed into corrugation shape initially by semi-circular die, as shown in figure 2.2.3 left, then straightened by pressing the corrugation-shaped part using two flat platens, as shown in figure 2.2.3 right. By repetitively bending and straightening the material without any significant change in cross-section, a large

amount of strain can be introduced in the material, further achieving the grain refinement [21]. The effective strain through the RCS process, ε_{eff}, is follow the equation below [20],

$$\varepsilon_{eff} = n\frac{4}{3}\ln\left(\frac{r+t}{r+0.5t}\right) \quad (4)$$

whereε_{eff} n is the number of passes, r is the radius of the semi-circular die, and t is the thickness of the specimen. Although the large-scale production is one of the advantages of the RCS processing, homogeneity in the microstructure of the processed samples is still a critical problem to solve [14].

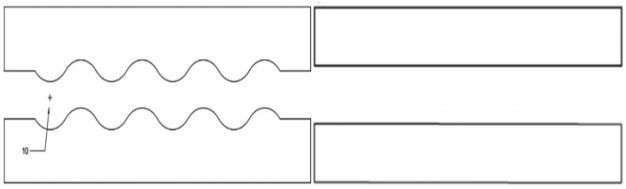

Figure 2.2.3 Schematic view of RCS. Left: corrugation process. Right: straightening process [20].

High-pressure torsion (HPT) is a metal processing technique which involves torsional straining under severe hydrostatic compressive pressure to the materials. Figure 2.2.4 [22] shows a schematic drawing of the principles of HPT, where the upper and lower anvils provide these shear and compressive straining to the disk-shape sample. In practice, HPT processing is recognized as one of the most effective SPD procedures for producing the finest grain sizes in metallic materials. Thus, the present study utilizes the HPT process as a metal processing tool, and the detailed HPT processing is described in the following section.

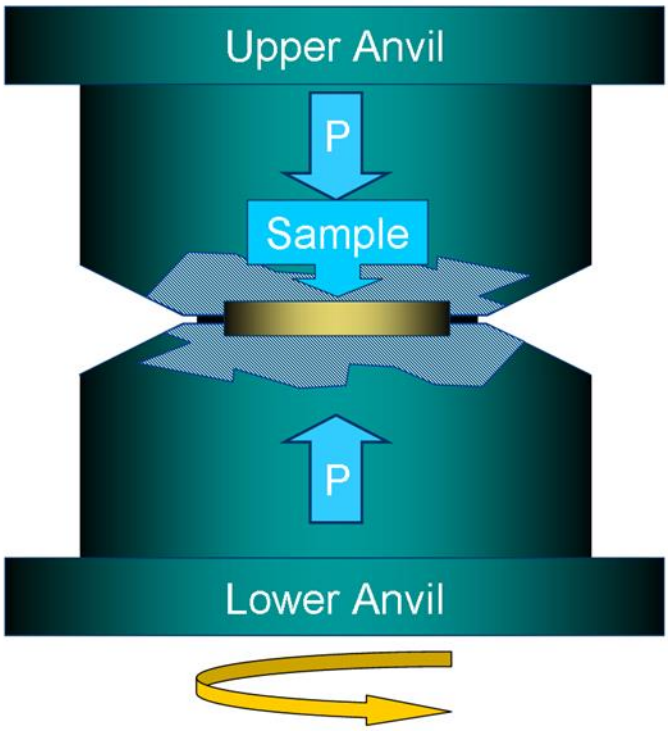

Figure 2.2.4. The schematic view of HPT [22]

2.3 High-Pressure Torsion

The development of HPT process is based on Nobel Laureate Professor P.W. Bridgman's early work about the metal processing with hydrostatic pressure and torsion [13]. There are three different types of HPT configuration, which are illustrated schematically in Figure 2.3.1 [23].

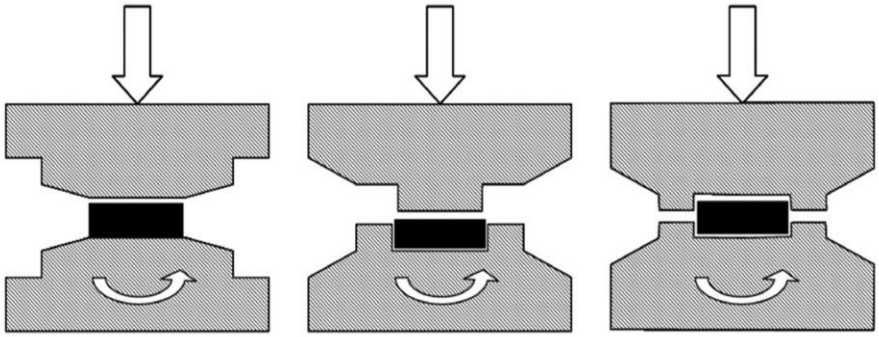

(a) (b) (c)

Figure 2.3.1 Schematic view of three different anvil configurations for HPT processing, (a) unconstrained, (b) constrained and (c) quasi-constrained conditions [23]

All these three HPT processes apply severe pressure to a material in a disk shape, which is compressed by two anvils where the bottom anvil rotates concurrently at a steady rate. The unconstrained HPT set, shown in Figure 2.3.1 (a), allows the material to free flow outward during the process leading to a significant volume loss of the material. To resolve the problem of free flow, the constrained HPT set-up was developed as shown in Figure 2.3.1 (b). The metal disk is placed into the cavity in the bottom anvil, where the depth of the cavity is equal to or more than the thickness of the disk. During applying the compressive pressure by pressing the sample with the upper plunger (or anvil) and concurrent torsion straining by rotating the lower anvil, the material is completely constrained without any free flow. However, this constrained

design causes the increase of friction between the material and cylindrical wall that subsequently causes inevitable heat. Thus, the quasi-constrained design, as shown in Figure 2.3.1 (c), is developed as the ultimate solution to introduce the severe compressive and torsional strain while maintaining the sample volume without generating any heat [22]. It should be noted that, since the disk sample is kept constant during the quasi-constrained HPT process, the continuous torsional turns can be applied for increasing accumulative strain within the sample.

In practice, HPT processing introduces simple shear with shear strain, γ, within a disk sample and it is given by the equation below:

$$\gamma = \frac{2\pi N r}{h} \tag{5}$$

where *N* is the number of torsional turns, *r* is the radial distance from the disk center where *r* = 0, and *h* is the sample thickness. In case of the pure shear stress, the equivalent strain ε_{eq} is further introduced by using the von-Mises expression [24]:

$$\varepsilon_{eq} = \frac{2\pi N r}{\sqrt{3} h} \tag{6}$$

Thus, the equations (5) and (6) suggest that even for the same amount of the rotation the induced strain varies along the disk radius, and the maximum strain will be achieved at the disk edge while the strain remains zero at the disk center. Therefore, the principles imply that the refined microstructure after HPT processing tends to be heterogeneous at any numbers of HPT turns. In general, most HPT samples are produced on disk samples having a disk diameter of 10 mm with thicknesses of 1.0 mm.

However, it is well recognized that after sufficient numbers of HPT turns the processed materials enable to show relatively homogeneous hardness, thus microstructure [25]. Figure

2.3.2 (a)-(d) shows representative hardness variations within a disk as well as the hardness evolution with increasing numbers of HPT turns for a Cu-Zr alloy after HPT for 1/4, 1, 5 and 10 turns, respectively [25]. From Figure 2.3.2 (a), the disk surface shows heterogeneous hardness distribution after 1/4 turn. The maximum hardness is observed at the periphery and the lowest hardness is recorded at the disk center. There is an apparent increase in hardness at the disk centers after 1 turn in Figure 2.3.2 (b), while there is little hardness improvement at the disk edges. After 5 and 10 turns in Figure 2.3.2 (c)-(d), the Cu-Zr disk achieves reasonably homogeneous hardness distributions across the disk diameters with ~160 to 170 Vickers microhardness.

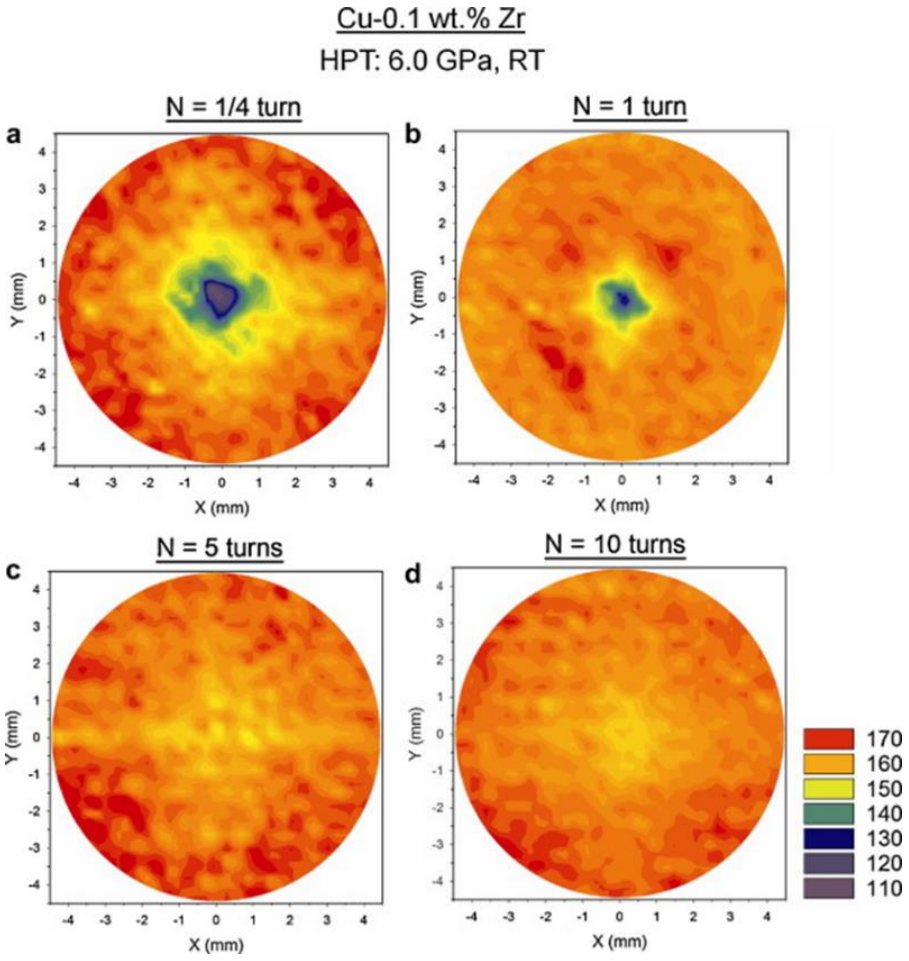

Figure 2.3.2 color-coded contour map for Cu-0.1wt.% Zr processed by HPT after (a)1/4 turn, (b) 1 turn, (c) 5 turns, (d) 10 turns. [25]

The following earlier experimental and computational modeling reports explained the hardness, thus microstructural, homogeneities within the processed materials with increasing numbers of HPT turns in terms of the accumulative equivalent strain:

1. Vorhauer and Pippan explained that, in practice, it is impossible to place the axes of anvils align ideally, further introducing the strain at the disk center [15].

2. Y. Estrin *et al.* explained the accumulation of equivalent strains at the disk centers by simulating the HPT process with two gradient plasticity models [26].

Besides the number of HPT turns, the applied pressure also affects the materials' hardness and microstructural homogeneity. Figure 2.3.3 is the plot of Vickers microhardness vs. distance from the disk center for an Al-3% Mg-0.2% Sc alloy after HPT for 5 turns under various pressures at 0.62, 1.25, 2.5 and 6.0 GPa [27]. It is obvious that the hardness increases with increasing the distance from the disk center for all processing pressure conditions, but the overall hardness increases and the differences in the hardness values within each disk are reduced with increasing the applied compressive pressure.

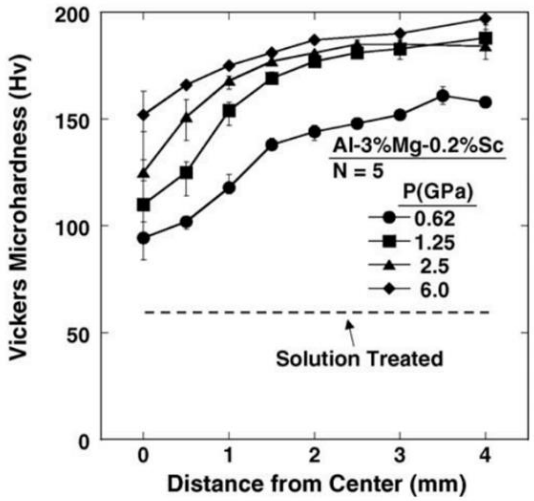

Figure 2.3.3 Vickers microhardness vs. Distance from disk center after 5 rotations [27]

From the earlier studies, it can be concluded that both rotational turns and applied pressure during HPT have significant effects on material's mechanical properties and hardness distributions. As the pressure and turns increase, materials generally show a higher level of hardness due to the significant grain refinement and achieve the homogeneous hardness and microstructural homogeneities. From such previous reports, it is recognized that a compressive pressure of 6 GPa and 5 or higher turns during HPT process are necessary to achieve the homogeneously high hardness/microstructure in most metals and alloys.

Other than hardness, ductility is also an important property to analyze for UFG materials processed by HPT. It is common to apply conventional tensile testing to analyze the ductility of conventional materials having large volumes. However, the conventional testing technique is not suitable for the HPT samples with the current lab-scale sizes. As was mentioned earlier, the current lab-scale HPT samples are too small to be applied for the conventional tensile machines by applying ASTM standards. Therefore, a novel technique of nanoindentation is found useful on the HPT processed samples instead of the conventional tensile tests.

Figure 2.3.4 shows a representative load-displacement (*P*-*h*) curve for a CoCrFeNiMn high-entropy alloy without HPT and after HPT for $N = 2$ turns at 6 GPa and tested at four different nanoindentation strain rates [28]. The recorded displacements decreased after HPT represents the increasing hardness in the alloy after processing. Moreover, both material conditions show a consistent trend of decreasing displacements with increasing strain rates leading to positive strain rate sensitivity in the alloy with/without HPT. The detailed study of plasticity can be analyzed by evaluating the strain rate sensitivity, and the present research will demonstrate such analysis in the following results and discussion section. The inset shows the load-displacement (*P*-*h*) curves for the specimen processed by different HPT turns under the

same strain rate. Accompanied by the increasing number of rotations, a significant hardness evolution is observed from the plot, which is the same as in the previous discussion [28].

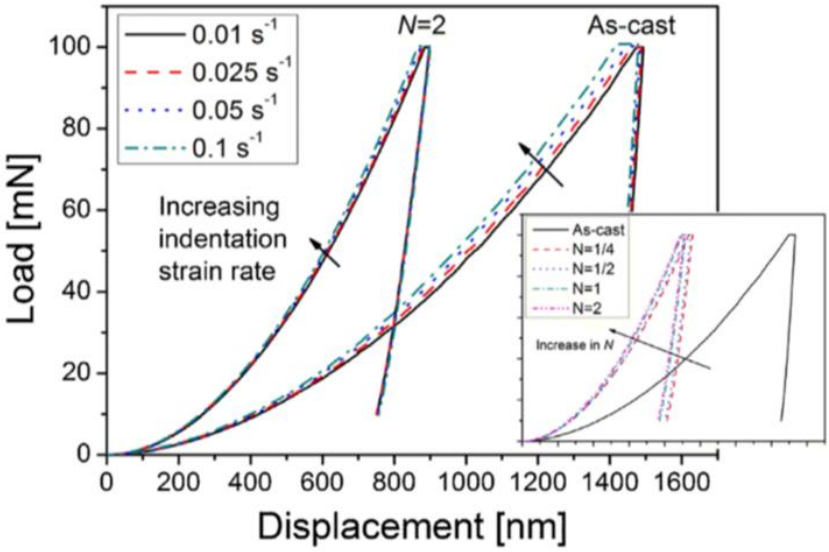

Figure 2.3.4 Load-displacement curves of CoCrFeNiMn HEA with different strain rates, inset is the test for materials processed by different HPT turns under the same strain rate [28].

It is worthwhile to note that there is a limited study demonstrating conventional tensile testing on the HPT-processed samples, while the tensile samples will be a miniature size. Figure 2.3.5 is the schematic view of an HPT-processed sample [27] where a right half of the disk provides the schematic illustration of a miniature specimen for tensile testing, while on the bottom-left, the area is used for a TEM specimen, and the hardness tests are conducted along the disk diameter. Therefore, it is apparent that the tensile test specimen is much smaller than the regular tensile test specimen. According to the previous report, the tensile test specimens with very small cross-sections generally show less ductility than larger specimens [29]. Moreover, the miniature tensile tests cannot capture the mechanical properties at the local region where the HPT-processed specimens after lower numbers of turns often include heterogeneous microstructure as expressed theoretically in equations (5) and (6).

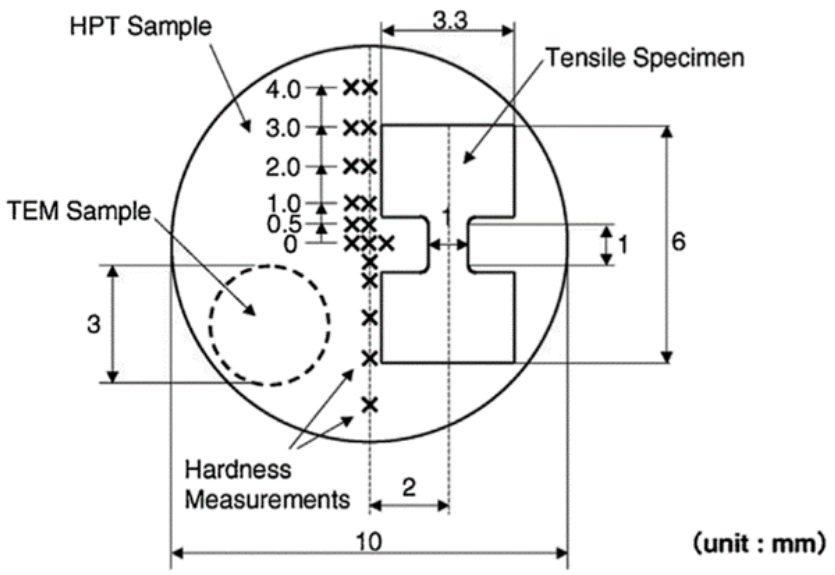

Figure 2.3.5 Schematic illustration of the test location on an HPT sample [27].

2.4 High-Entropy Alloy

Conventional metal alloys are based on one primary element, such as Al based alloys, Ni based alloys. Empirically, the configuration entropy change reaches to *R* during the formation of a solid solution, where *R* is the gas constant. Nevertheless, the novel alloys are designed as 5 or more elements in equimolar or near equimolar, which can achieve more than 1.61 *R* as the configuration entropy change; these alloys are called high-entropy alloys (HEAs). Due to the large change in the configuration entropy, HEAs tend to form a single phase microstructure with simple crystalline structures, such as f.c.c. and b.c.c., having better mechanical properties, including high stability and high strength than conventional alloys [30].

HEAs can be processed by many different methods, such as Arc melting [30], Powder bed fusion [31], Bridgman solidification [32], and thermal-spray [33], etc. Numerous earlier reports demonstrated that the mechanical properties of HEAs are dominated by the crystal structure. In practice, HEAs with b.c.c. structure tend to show high yield strength and low ductility, while HEAs with f.c.c. structure usually show reasonably high yield strength as well as high ductility [34, 35]. Among many studied HEAs and elevated-entropy alloys, CoCrFeNi and HfNbTiZr are well known f.c.c. and b.c.c. structured alloys, respectively.

These particular elevated-entropy alloys are studied due not only to their stable simple structure attributing to the sluggish diffusion but also to their excellent and controllable properties by adding additional elements. For instance, addition of an element, Mn, in a CoCrFeNi f.c.c. HEA demonstrates strong temperature dependencies in the yield strength, and flow stress [36], and outstanding ductility compare to conventional f.c.c. alloys [37]. An HfNbTiZr b.b.c. HEA has been reported as the base alloy for many refractory materials and

exhibits good phase stability at high temperatures [38]. Furthermore, by adding other elements such as Al, the strength of the alloy significantly increases [39].

Besides the compositional elements and crystalline structure, grain size is another important factor for enhancing the mechanical properties of HEAs. Figure 2.4.1 shows an earlier example demonstrated by the stress-strain curves for a CoCrFeNiMn HEA having different grain sizes from 88.9 μm to ~500 nm [40]. The different grain sizes were obtained by cold rolling and further annealing at temperatures ranging from 650℃ to 1100℃ for 30 minutes. The samples with the grain size of 88.9 μm and 62 μm are treated by annealing at 1200℃ and 1100℃ for 60 minutes, respectively [40].

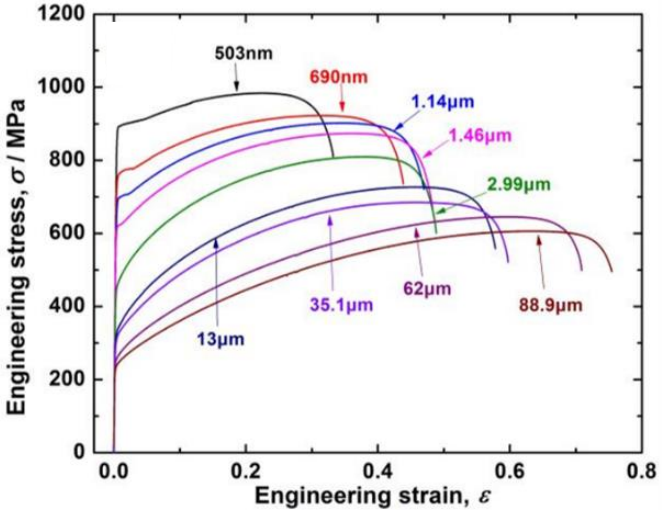

Figure 2.4.1 Stress strain curve of CoCrFeNiMn HEA with different grain sizes [40].

It is seen in Figure 2.4.1 that as grain size decreases the CoCrFeNiMn HEA shows higher yield strength, which matches with the principle of Hall-Petch strengthening. Therefore, the application of HPT processing on HEAs will further refine the grain size of the HEAs and it is anticipated to introduce better mechanical properties.

Accordingly, the present research applies HPT on the as-cast CoCrFeNi and HfNbTiZr, and additive-manufactured CoCrFeNi HEAs. Their hardness and microstructural evolution, texture change, and mechanical responses will be evaluated with applying different numbers of HPT conditions.

3 Experimental Procedures

3.1 Materials and Sample Preparation

The materials used in this research were as follows: as-cast CoCrFeNi with 25 at.% for each element, as-cast HfNbTiZr with 25 at.% for each element, and additive manufactured CoCrFeNi with the atomic fractions of 23 at.% Co, 21 at.% Cr, 21 at.% Fe, and 35 at.% Ni.

The as-cast CoCrFeNi HEA was prepared by vacuum induction melting and drop-casting of a mixture of pure metals (purity >99.9 wt.%). The cast ingot with the thickness of ~39 mm was hot-rolled at 1050 °C to a thickness of ~14 mm, which corresponds to a thickness reduction of ~64% followed by homogenization at 1100 °C for 1 h. The as-cast HfNbTiZr HEA was synthesized by magnetic levitation melting of a mixture of the four pure components (purity >99.9 wt.%), followed by solid solution treatment at 1290 °C for 24 h.

The CrFeCoNi HEA powders were produced by the spraying method. The solid HEA alloy was produced by Powder Bed Fusion technology with a laser heat source (PBF-L) using a metal 3D printer, Trumpf TruPrint 1000. The billet samples were printed as bars where the length is parallel to the build direction with a cross-section having a diameter of 12.0 mm. The applied parameters for the printing process were a laser power of 150 W, a laser speed of 600 mm/s, a laser spot diameter of 55 µm, a hatch spacing of 50 µm, and a layer thickness of 20 µm. The printing process was performed in an inert atmosphere (Ar) with a gas feed velocity of 2.5 m/s and a chamber pressure of 1 bar. The oxygen level was within 0.3 at.%. Figure 3.1.1 shows (a) a scanning electron microscopy (SEM) micrograph showing the morphology of the HEA powders and (b) a plot showing the powder size distributions for the powder HEA before

printing [31]. According to figure 3.1.1 (b), the particle size diverse from 20 to 65 µm and an average particle size of 35-40 µm.

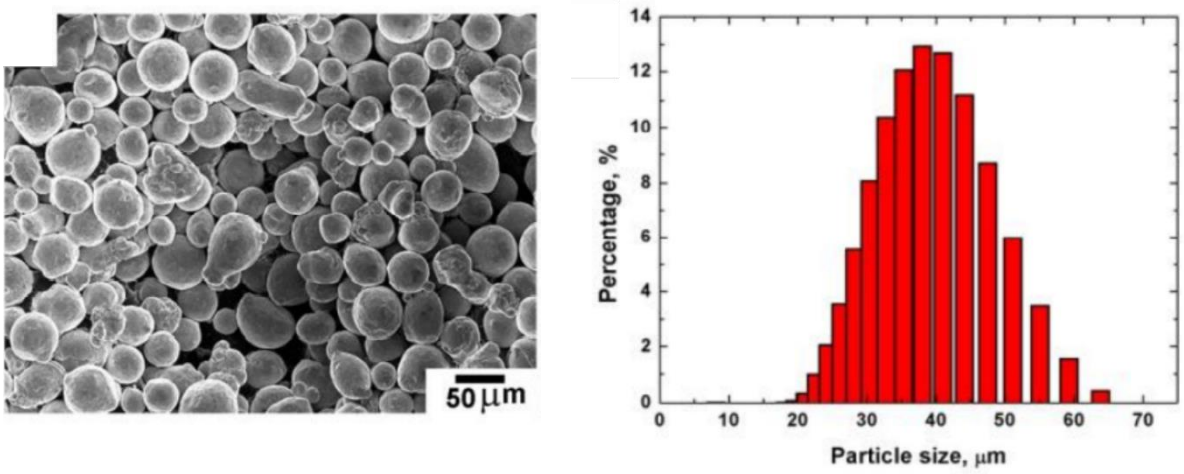

(a) (b)

Figure 3.1.1 (a) a scanning electron microscopy (SEM) micrograph showing the morphology of the HEA powders and (b) a plot of the powder size distributions for the powder HEA before printing [31].

The as-cast HEA samples in a bar shape with 10 mm diameter were cut into disks with thicknesses ~1 mm by using a diamond cutting saw. A large diameter of 12.0 mm for the 3D-printed billets was first ground to have a 10.0 mm diameter and then sliced by the cutting saw for HPT processing. All disk samples were ground by using an MTDI MPE series dual-table polisher to obtain the disks with a thickness of ~0.80 mm, which is the standard sample dimension for this study.

3.2 Materials Processing

The disks with a diameter of 10.0 mm and a thickness of 0.80 mm were processed by the HPT facility at room temperature with the quasi-constrained condition as shown in Figure 2.3.1(c). Figure 3.2.1 shows an actual HPT machine used in this study. A disk sample was placed in the cavity of the bottom anvil, the anvil then moving upward, applied a compressive pressure of 6.0 GPa to the material, which caused a visible outflow of the material. Concurrently, the bottom anvil rotated at 1 rotation per minute (rpm), introducing the shear strain to the sample disk. In order to evaluate the evolution of structural and mechanical properties, a series of numbers of HPT turns, N, were applied to the sets of HEAs.

Figure 3.2.1 A photograph of the HPT facility used in this experiment.

Subsequently, the HPT-processed disks were cut into halves along the diameters and then were mold for polishing either sample surfaces or vertical cross-sections. These surfaces of the cut samples were ground by 800, 2000 grit silicon carbide papers, further polished by 0.5 μm alumina powders and 0.05 μm silica suspension with cotton cloths under an ethanol condition to remove the fine scratches and obtain mirror-like surfaces.

3.3 Structural Characterization

The optical micrographs and the Vickers microhardness were obtained using a Mitutoyo HM-200 automatic hardness testing system. A series of micrographs were taken under a magnification of 50× and stitched together for each sample. The Vickers microhardness values were recorded with the loads of 250 gf for the HPT-processed as-cast HfNbTiZr and both as-cast and 3D-printed CoCrFeNi through 1/2 turn and of 300 gf for both as-cast and 3D-printed CoCrFeNi for more than 1 turn. The individual hardness value was recorded in two different ways, which are shown in Figure 3.3.1, where one way uses (a) a rectilinear grid pattern with an interspace of 0.25 mm for the as-cast samples, and the other uses (b) a 5-line pattern on cross-sectional planes with a distance of 0.12 mm for the 3D-printed samples.

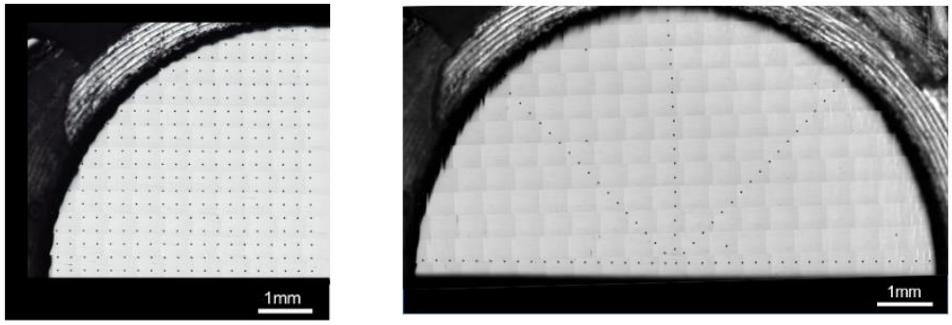

(a) (b)

Figure 3.3.1. (a) rectilinear grid pattern, and (b) 5-line pattern

The sample surfaces after hardness testing were re-polished mechanically by using 2000 grit silicon carbide papers to remove the indentation marks on the surfaces for further investigations for X-ray diffraction (XRD) peak profile analysis. The XRD analysis was performed using Bruker-AXS D8 Discover on each re-polished disk sample surface. The experiments used CuKα as the radiation source, with a step size of 0.04°, a scan speed of

3° per minute, and the peak range from 30° to 100°. For Micro-XRD analysis, the XRD analysis was conducted at an examination area of 1 mm^2 on the disk centers and edges of the samples. An analytical software package of Materials Analysis Using Diffraction (MAUD) [41], which is based on the Rietveld method, was used to identify and quantify the amounts of compounds from these XRD profiles.

3.4 Collaboration Work

The microstructure was observed using high resolution transmission electron microscopy (HRTEM-PhilipsCM200 and Philips C2100 at an accelerating voltage of 200 kV). Conventional mechanical polishing was applied to prepare TEM samples. The samples were first cut and then ground to a thickness of lower than 100μm using 1000 abrasive paper. A series of 3 mm disks were punched out at *r* of ~3.5 mm in each disk sample. Using diamond paste, the punched samples were then polished and ion milling was applied for thinning in the final step.

The nanoindentation tests were performed at Hanyang University, South Korea, as a collaboration work. The micro-mechanical properties were examined at the disk edges with a nanoindentation facility, Nanoindenter-XP (formerly MTS; now Keysight, Santa Rosa, CA), with a three-sided pyramidal Berkovich indenter having an angle between the centerline to the three faces of 65.3°. For all testing conditions, at least 20 indentations were conducted to provide statistically valid data. All measurements were operated under a predetermined maximum peak load of $P_{max} = 50$ mN at the constant indentation strain rates of 0.0125, 0.025, 0.05 and 0.1 s^{-1}.

4 Results

4.1 Vickers microhardness Measurement

Variations in hardness on the disk surfaces are shown in Figure 4.1.1, where the Vickers microhardness values are plotted against the distance from the disk center for (a) as-cast CoCrFeNi and (b) as-cast HfNbTiZr alloys in an as-received condition and after HPT for 1/2 turn and 5 turns. It should be noted that due to the principles of HPT processing, as shown in Section 2.3, the evolution of hardness, thus microstructure, is always radial symmetry in the HPT-processed disks as was demonstrated in Fig. 2.3.2.

Figure 4.1.1 (a) shows the Vickers microhardness value of ~160 for the as-cast CoCrFeNi alloy before processing, and the hardness distributes homogeneously along the radius of the disk surface, thereby demonstrating the structural homogeneity in the material. After processed by HPT for 1/2 turn, a significant hardness increase can be found from 160 to 375 at the disk center. In the meanwhile, an apparent hardness increase from 375 to 520 can be observed from the disk center towards the disk edge on the disk surface after HPT for 1/2 turn. The gradual hardness increase within the sample volume indirectly shows a microstructural gradation in the material after 1/2 turn by the HPT process. Further straining through 5 turns by HPT introduced the homogeneous hardness distribution with achieving saturated high hardness of ~525 along the disk radius. The saturated high hardness achieved by 5 HPT turns is consistent with the hardness at the disk edge after 1/2 HPT turn, and thereby it is confirmed that high numbers of HPT turn such as 5 turns are required to introduce homogeneous distributions of hardness, thus microstructure, in the HEA.

The as-cast HfNbTiZr alloy shows the hardness value of ~250 before HPT processing, as shown in Figure 4.1.1(b). After 1/2 turn of rotation by HPT under 6.0 GPa, the hardness increased to 290 at the disk center where r = 0 mm, and the hardness reaches close to the saturated hardness of >350 at the disk edge. After 5 turns, the material shows a reasonably homogenous hardness distribution at ~370 with slightly lower hardness towards ~350 at r <0.5 mm at the disk center. Thus, it confirms again that the HPT process for 5 turns or higher provides sufficient plastic deformation to the HEAs having different initial hardness by grain refinement leading to high hardness over the HEAs disk surfaces. It should be noted that the HfNbTiZr HEA has higher initial hardness than the CoCrFeNi HEA in the as-cast conditions, but recorded the lower saturated hardness after HPT for 5 turns. This may be attributed to the different crystal structures where the CoCrFeNi alloy has an f.c.c. structure [42] while the HfNbTiZr alloy has a b.c.c structure [43].

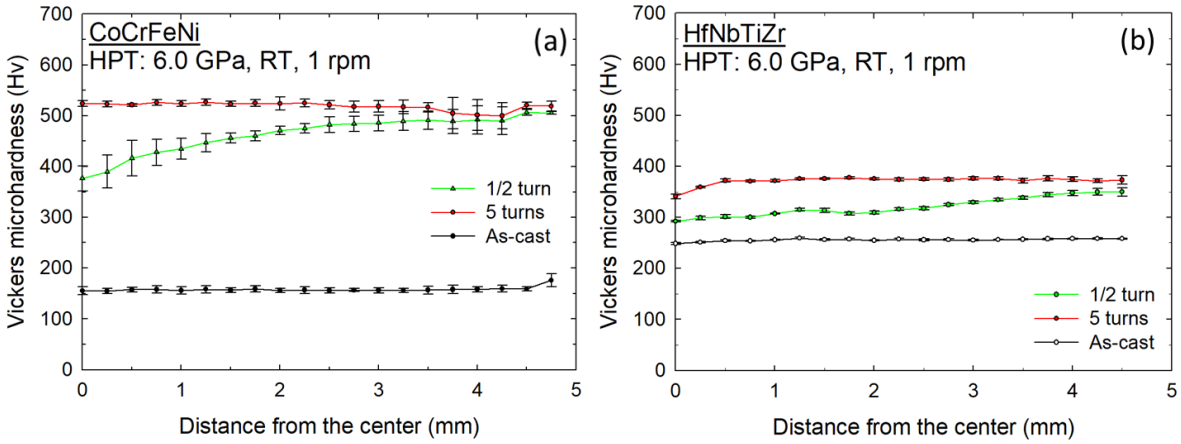

(a) (b)

Figure 4.1.1 Hardness distributions along the disk radius for (a) CoCrFeNi and (b) HfNbTiZr

Figure 4.1.2 shows the Vickers hardness distribution for the 3D-printed CoCrFeNi alloy. Specifically, the hardness values are measured along the diameters on the vertical cross-sections in an as-built condition, and after 1/2 turn, 1 turn, 2 turns, 4 turns and 8 turns by HPT processing.

The Vickers hardness value before HPT processing was ~250, which is higher than the alloy in the as-cast condition, as shown in Fig. 4.1.1(a). This could be caused by the initial sample condition where the alloy was built from powders having small particle sizes by the 3D-printed technique. Increasing numbers of HPT turns, the hardness evolution shows the same trend as was shown in the as-cast CoCrFeNi alloy where the hardness at the disk centers increases gradually to achieve high saturated hardness that is achieved in an early stage of deformation through 1/2 turn at the disk edges. After 4-8 turns by HPT, the Vickers microhardness values achieved the upper limit of 525 along the disk diameters. It should be emphasized that the hardness value of 525 is consistent with ~520 for the HPT-processed as-cast CoCrFeNi alloy, as shown in Fig. 4.1.1(a). Thus, these results suggest that the CoCrFeNi HEAs produced by different procedures enable the demonstration of the upper hardness limit with the Vickers hardness value of 525 after severe deformation by sufficient HPT turns.

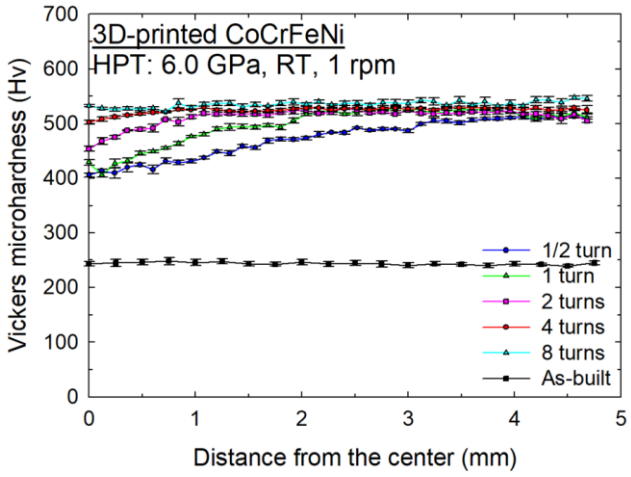

Figure 4.1.2 Hardness distribution along the diameters on the vertical cross-sections for the 3D-printed CoCrFeNi alloy after HPT processing.

In order to confirm the hardness evolution which is in radial symmetry within the disks after HPT for the HEAs, the color-coded contour maps are constructed for better visualization of

hardness on the sample surfaces of (a) as-cast CoCrFeNi and (b) as-cast HfNbTiZr alloys before HPT and after HPT for 1/2 turn and 5 turns in Figure 4.1.3 and on the vertical cross-sections of the cross-sections for 3D-printed CoCrFeNi alloy after HPT for 1/2, 1, 2, 4, 8 turns in Figure 4.1.4. The hardness color key is listed at the bottom right in each figure.

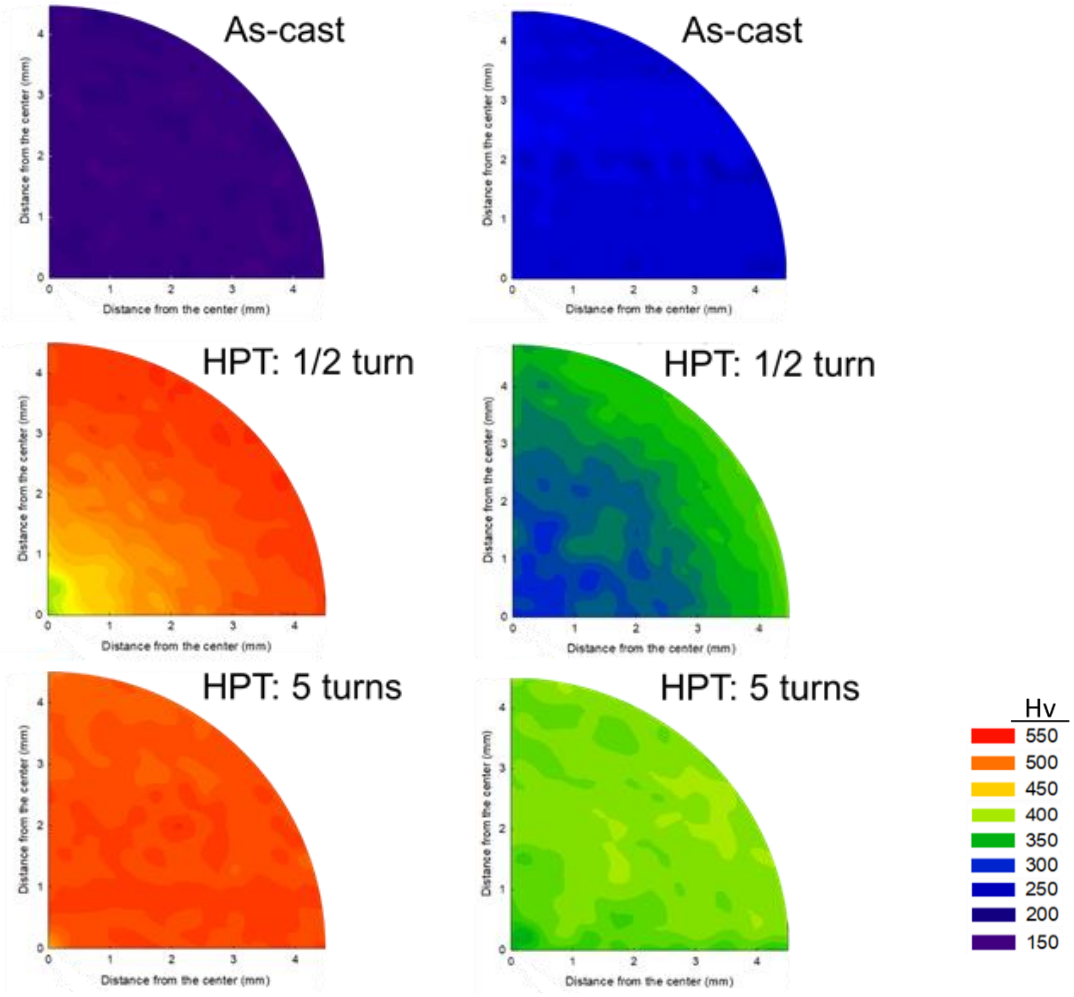

(a) (b)

Figure 4.1.3 The color-coded contour map of hardness distribution on the sample surface for (a) as-cast CoCrFeNi and (b) as-cast HfNbTiZr alloys before and after HPT.

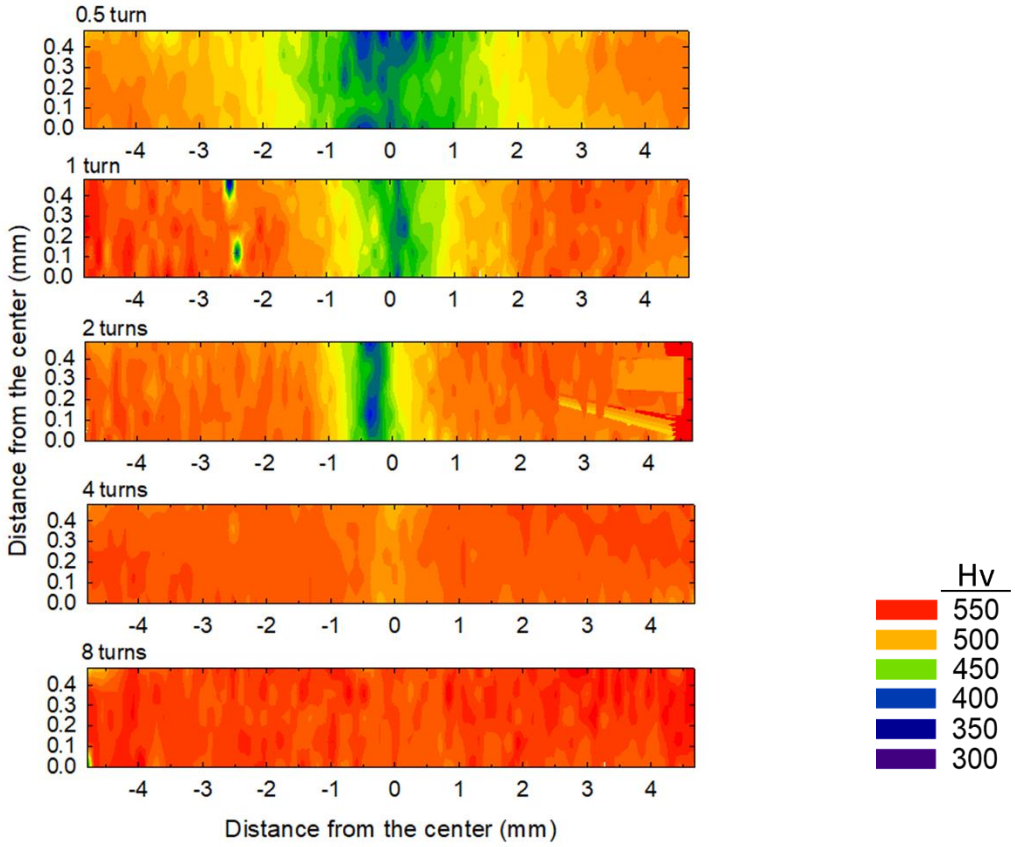

Figure 4.1.4 The color-coded contour maps showing the hardness distributions on the cross-sections for 3D-printed CoCrFeNi alloy after HPT.

It is apparent from Figure 4.1.3 that both as-cast HEAs show the hardness changes, which are radial symmetry. These color contour maps visualize that both HEA alloys demonstrated reasonable hardness homogeneity having an upper limit of hardness over the disk surfaces after HPT for 5 turns.

The hardness maps on the vertical cross-sections in Figure 4.1.4 also provide a clear visualization of the radial symmetry of the hardness evolution in the 3D-printed CoCrFeNi alloys. In addition, the hardness maps on the vertical cross-sections demonstrate the hardness homogeneity at any stage of HPT through the hardness saturation within the disk thicknesses.

4.2 X-ray Diffraction

Figure 4.2.1 shows the XRD line profiles for the 3D-printed CoCrFeNi alloy under different processing stages, where the Y axis gives the modified intensity and the X axis gives the 2θ value. The XRD line profiles are shown, from top to bottom, for the powder sample, as-built sample, the alloy after HPT for 1/2, 1, 2, 4 and 8 turns, respectively.

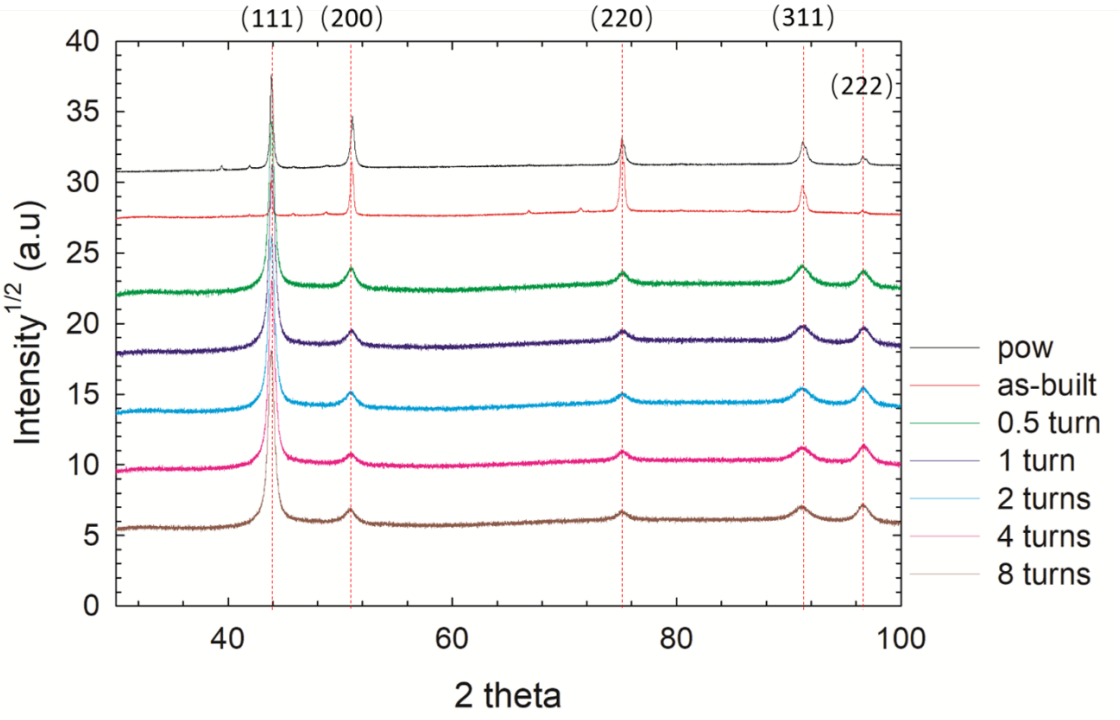

Figure 4.2.1 Combined X-ray diffraction line profiles for the 3D-printed CoCrFeNi alloy under different processing conditions with intensity vs 2 theta.

The influence of the wavelength from different quantum beam sources can be removed by the normalization of the raw XRD data by calculating the scattering vector, Q, with the equation of $Q = \frac{4\pi \sin(\theta)}{\lambda}$. The normalized plot of the XRD line profiles are shown in Figure 4.2.2. This normalization may not be critical in this study. However, for a future study of applying neutron and synchrotron analyses on the alloys and comparing the results, it is

reasonable to normalize the present data from XRD as well as the future results from the different quantum beam techniques, so that the normalized results can be compared directly in a plot. Thus, in this study, Figure 4.2.1 and Figure 4.2.2 show the equivalent results.

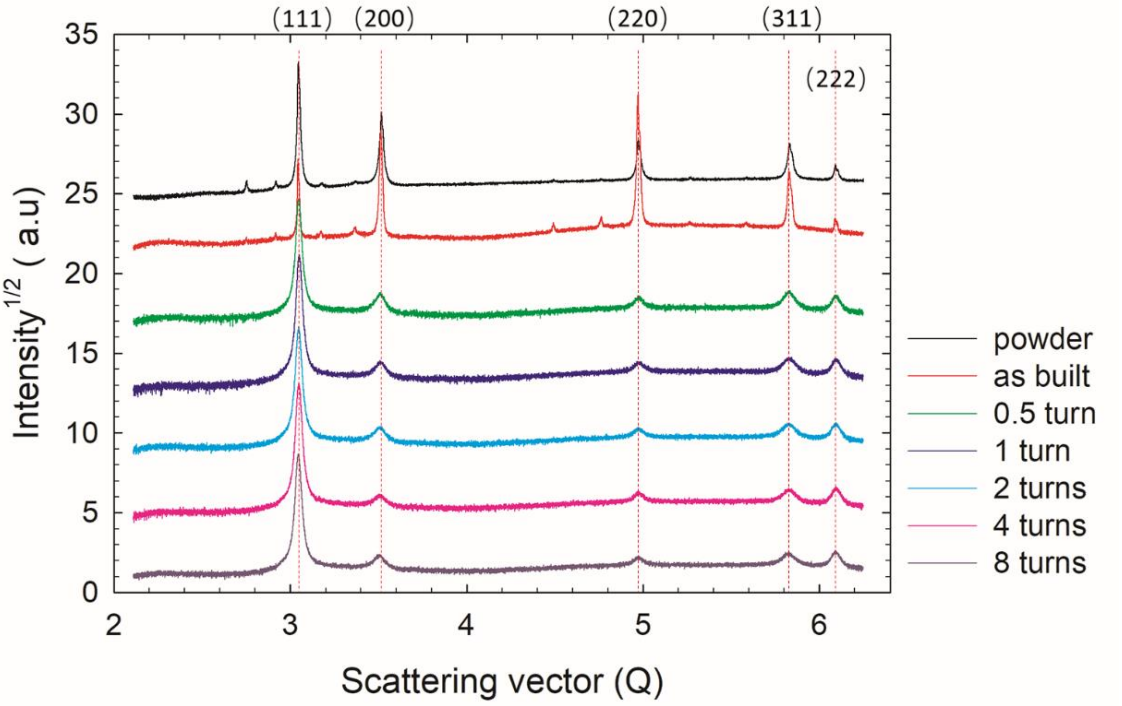

Figure 4.2.2 Normalized X-ray diffraction line profiles for the 3D-printed CoCrFeNi alloy under different processing conditions with intensity vs Scattering vector, Q.

The XRD patterns show a typical trend of an f.c.c crystal structure for the 3D-printed CoCrFeNi alloy under any sample conditions, and it is anticipated by the combination of these solute elements. There are three important findings in the XRD analysis. First, the texture change after the HEA powder is additively manufactured to the solid material where the Bragg reflections at 200 and 220 are stronger after 3D-printing. Then its further changes after HPT processing where there is a strong texture with the Bragg reflections at 111. Second, the texture after HPT is consistent with increasing numbers of turns. Thus, the early stage of HPT for less than 1/2 turn has introduced the final texture of the HPT-processed HPA. Third, the HPT

processed samples show apparent peak broadening, which may be attributed to the grain size refinement, and it is a general trend in UFG materials processed by HPT [44].

Our earlier collaborative study reported the XRD line profiles for the as-cast CoCrFeNi alloy after HPT for 10 turns [42] and the as-cast HfNbTiZr alloy after HPT for 20 turns [43], and these are shown in Figure 4.2.3 (a) and (b), respectively. It is reasonable to consider that these HPT turns are high enough to form stable saturated ultrafine-grained microstructures, as was concluded in the hardness experiments in the present study. It is apparent that the XRD plots define an f.c.c structure for the CoCrFeNi alloy and a b.c.c structure for the HfNbTiZr alloy.

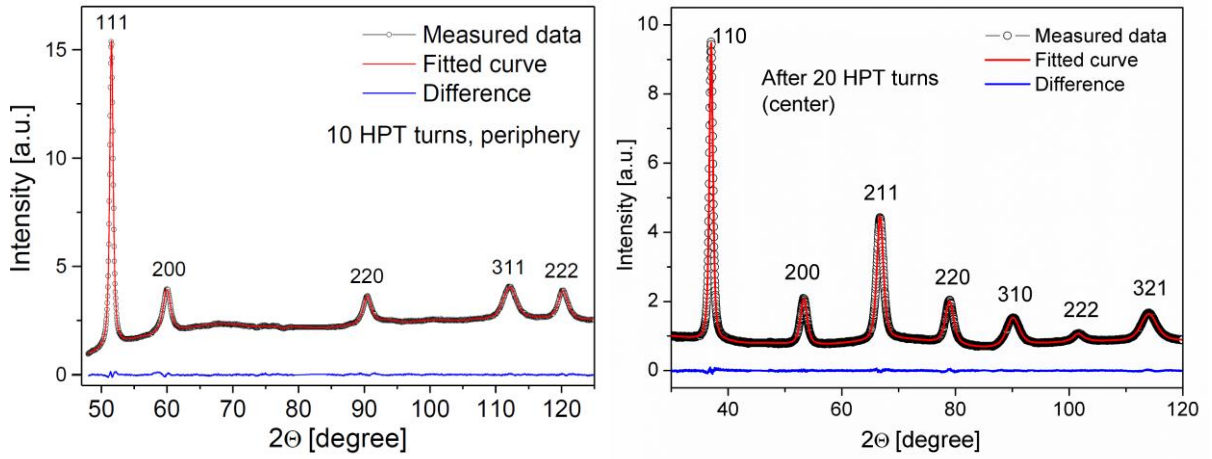

(a) (b)

Figure 4.2.3 X-ray diffraction line profiles for the as-cast CoCrFeNi alloy after HPT for 10 turns [42] and the as-cast HfNbTiZr alloy after HPT for 20 turns [43].

4.3 Nanoindentation

Figures 4.3.1- 4.3.3 are a series of plots showing the load-displacement curves for the as-cast CoCrFeNi alloy after HPT for 5 turns, 3D-printed CoCrFeNi alloy in an as-built condition, and 3D-printed CoCrFeNi alloy after HPT for 8 turns, respectively. Testing was conducted at the constant indentation strain rates of 0.0125, 0.025, 0.05 and 0.1 s^{-1}, which are equivalent to the uniaxial strain rates of (a) 1.25×10^{-4} s^{-1}, (b) 2.5×10^{-4} s^{-1}, (c) 5.0×10^{-4} s^{-1}, and (d) 1.0×10^{-3} s^{-1}, respectively, by applying the empirical relation between uniaxial strain rate, $\dot{\varepsilon}$, and of $\dot{\varepsilon} \approx 0.01\ \dot{\varepsilon}_i$ where $\dot{\varepsilon}_i$ is the indentation strain rate [45]. At each strain rate, 20 separate indentations are applied to acquire statistically validated data.

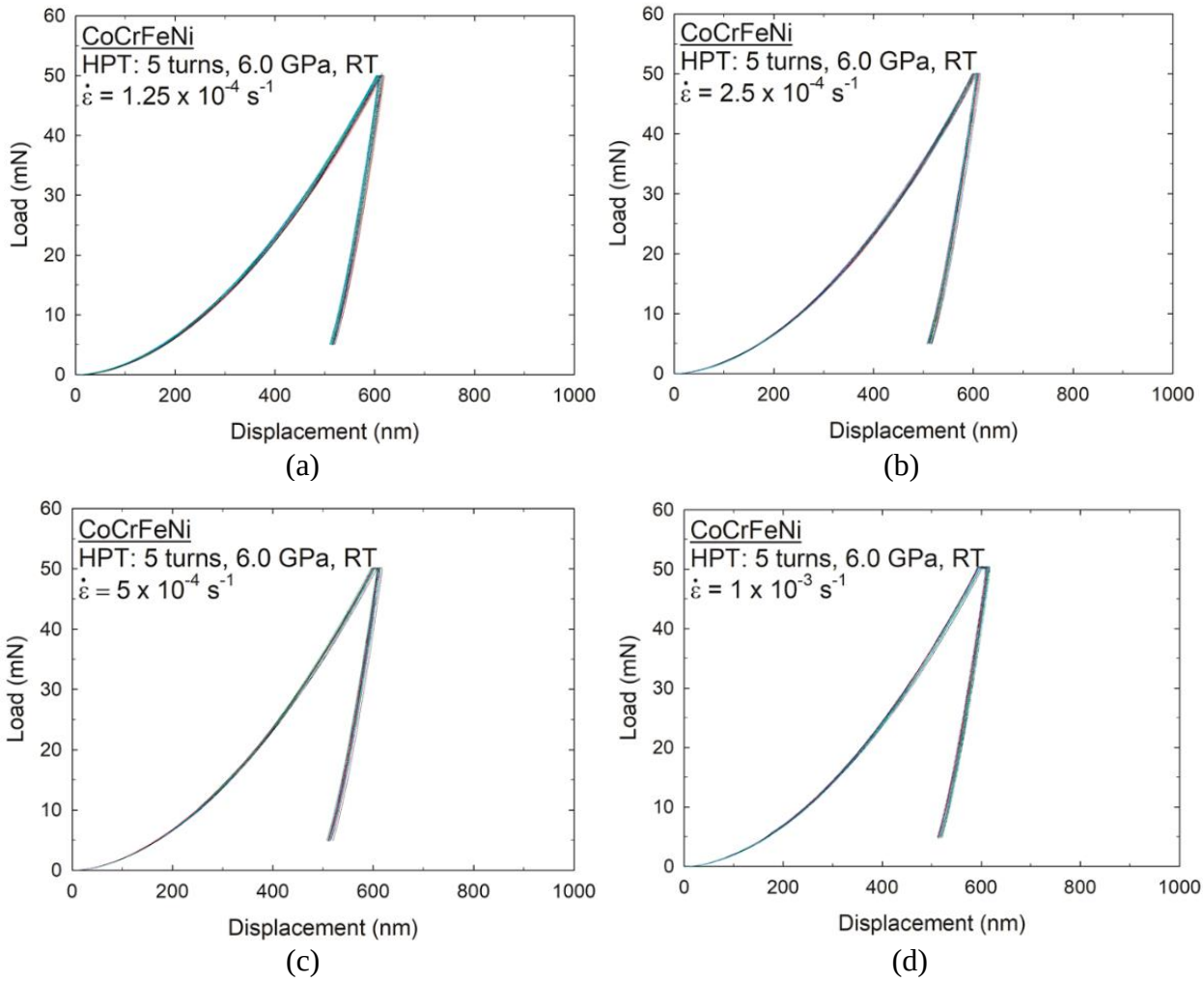

Figure 4.3.1 Load-displacement courves for the as-cast CoCrFeNi alloy after HPT for 5 turns tested at strain rates of (a) 1.25 × 10^{-4} s^{-1}, (b) 2.5 × 10^{-4} s^{-1}, (c) 5.0 × 10^{-4} s^{-1}, and (d) 1.0 × 10^{-3} s^{-1}

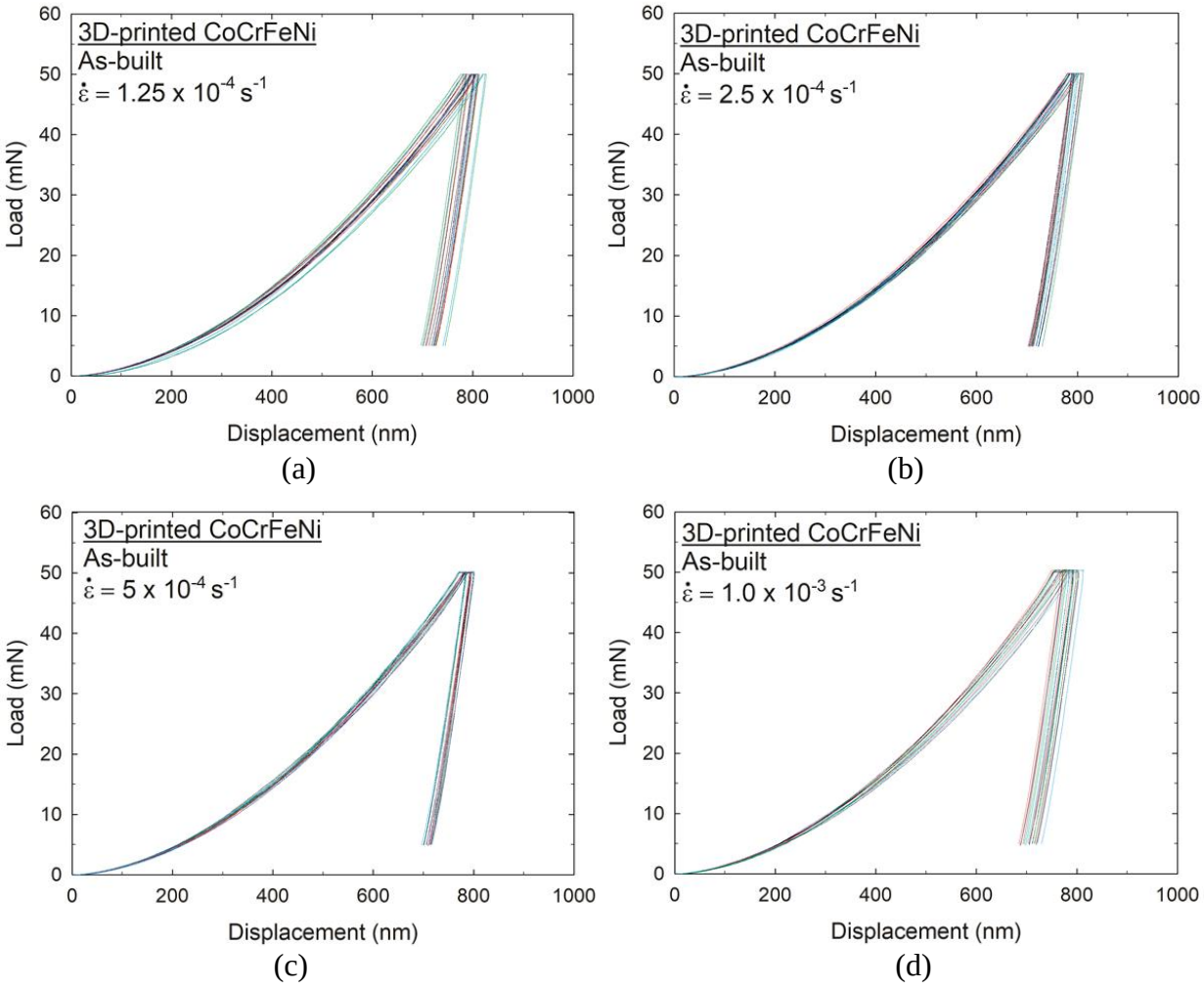

Figure 4.3.2 Load-displacement curves for the as-built 3D-printed CoCrFeNi alloy tested at strain rates of (a) 1.25 × 10^{-4} s^{-1}, (b) 2.5 × 10^{-4} s^{-1}, (c) 5.0 × 10^{-4} s^{-1}, and (d) 1.0 × 10^{-3} s^{-1}

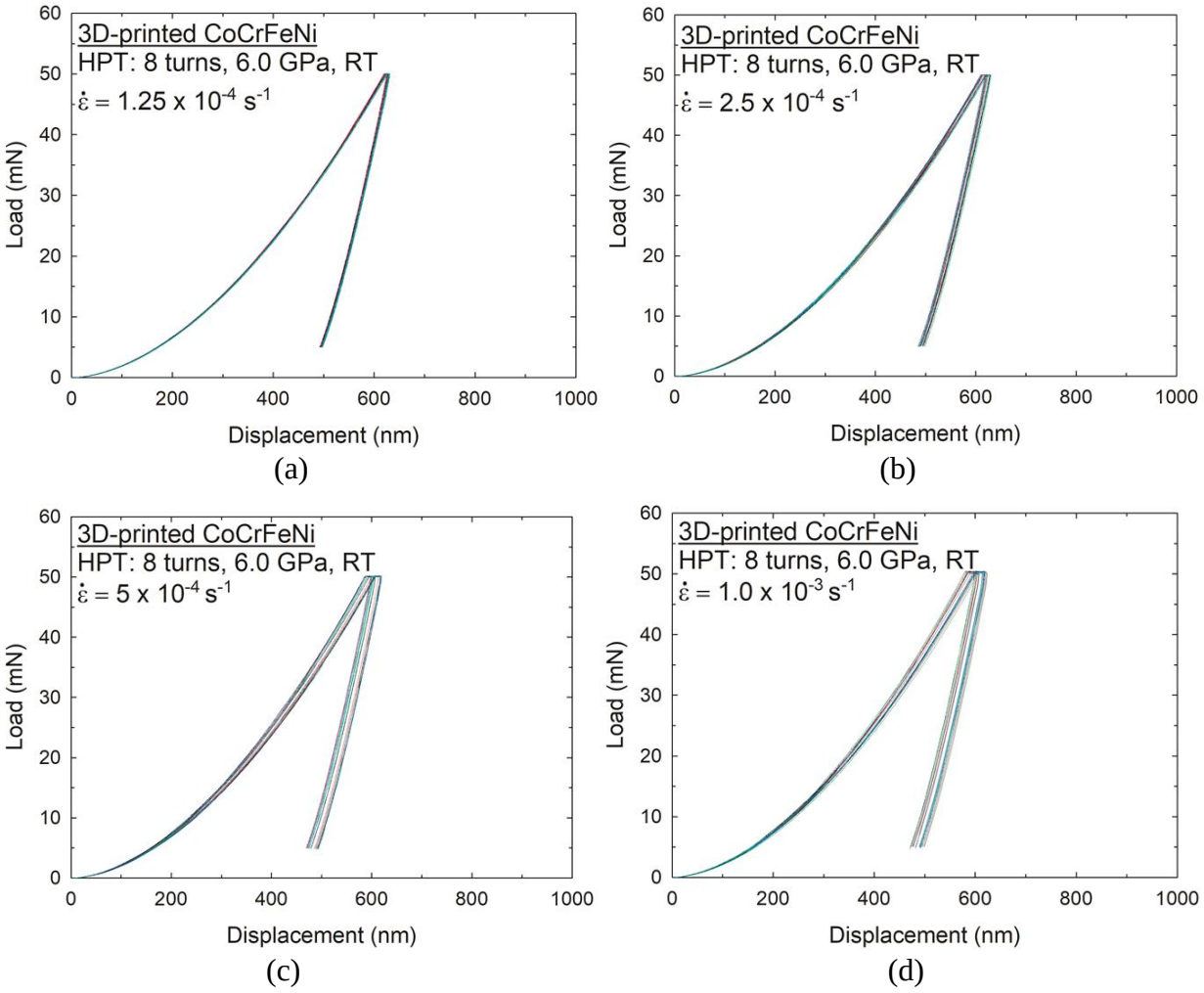

Figure 4.3.3 Load-displacement curves for the 3D-printed CoCrFeNi alloy after HPT for 8 turns tested at strain rates of (a) 1.25 × 10^{-4} s^{-1}, (b) 2.5 × 10^{-4} s^{-1}, (c) 5.0 × 10^{-4} s^{-1}, and (d) 1.0 × 10^{-3} s^{-1}

There are three important findings in the nanoindentation tests for the CoCrFeNi HEA. First, it is apparent from all figures that 20 separate measurements in each testing condition showed reasonable consistency in the HEA, while the alloy after HPT processing in Figures 4.3.1 and 4.3.3 shows higher consistency than the alloy without processing. It indicates that there is excellent plastic stability in nano- and micro-scale in these HPT processed HEA. Second, the load-displacement curves for the consistent element HEAs described that the as-built sample without HPT processing shows larger displacements than after HPT processing of both the as-

cast and 3-D printed alloys at all strain rates. Thus, the HEA without HPT processing demonstrated better ductility than the HEA after HPT processing, and it is anticipated from the Vickers microhardness results where the as-built material demonstrated the lowest hardness values among these three. Third, closer observation describes that the displacements are reasonably similar for the HPT-processed as-cast and 3D-printed HEAs at each strain rate. The result indicates the consistent strength at each indentation strain rate, and it is in excellent agreement with the finding after the Vickers microhardness tests noted in the earlier section.

Figure 4.3.4 shows the load-displacement curves for the as-cast HfNbTiZr alloy after HPT for 8 turns tested at the same testing condition by nanoindentation.

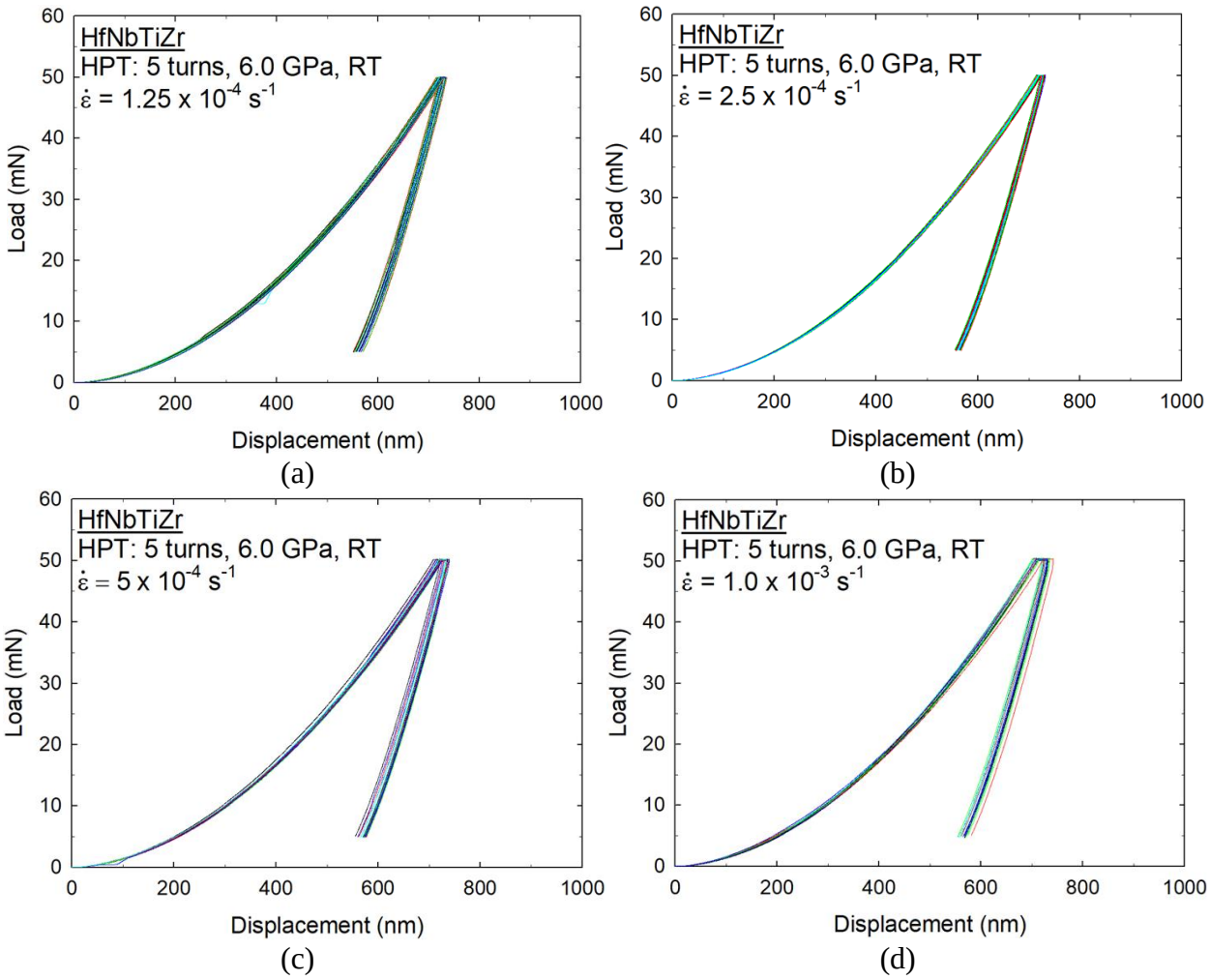

Figure 4.3.4 Load-Displacement curves for the as-cast HfNbTiZr alloy after HPT for 5 turns tested at strain rates of (a) 1.25 × 10^{-4} s^{-1}, (b) 2.5 × 10^{-4} s^{-1}, (c) 5.0 × 10^{-4} s^{-1}, and (d) 1.0 × 10^{-3} s^{-1}

The load-displacement curves show excellent consistency in the 20 separate measurements at each strain rate, thus implying the plastic stability of the as-cast HfNbTiZr HEA after HPT processing. It was demonstrated in the section 4.1 that the Vickers microhardness of the HPT-processed as-cast HfNbTiZr HEA showed lower hardness than the as-cast CoCrFeNi HEA after HPT. Thus, the anticipated result of larger displacement at all strain rates in the HPT-processed as-cast HfNbTiZr HEA when comparing Figure 4.3.4 with Figure 4.3.1.

4.4 Microstructure

Figure 4.4.1 shows the backscattered electron (BSE) images in (a) low and (b) high magnifications of the 3D-printed CoCrFeNi alloy after printing. These photos were taken on the sample surfaces vertical to the printing direction.

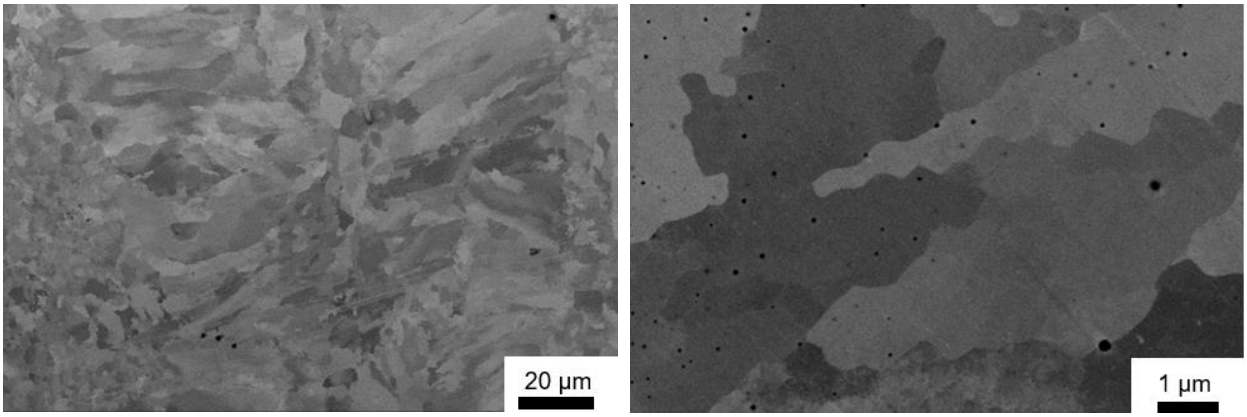

(a) (b)

Figure 4.4.1 Backscattered electron images of the as-built CrFeCoNi alloy before HPT processing.

Figure 4.4.1(a) shows the elongated domains, whose length correlates with the laser beam track length of 50 μm. A duplex microstructure comprising fine grains up to 10 μm in a phase size is observed in the middle between neighboring melt tracks. This appearance can be the result of the overlaps of the neighboring laser tracks, re-melting, and recrystallization. A typical cellular substructure for printing materials is displayed with elongated grains of ~1.0 μm of the as-built sample, as shown in Figure 4.4.1(b). Thus, the as-built samples demonstrated a bimodal grain size distribution of ~50 μm with 1.0 μm.

Figure 4.4.2 shows the TEM images of the 3D-printed CoCrFeNi alloy after HPT for (a) 1 turn and (b) 8 turns.

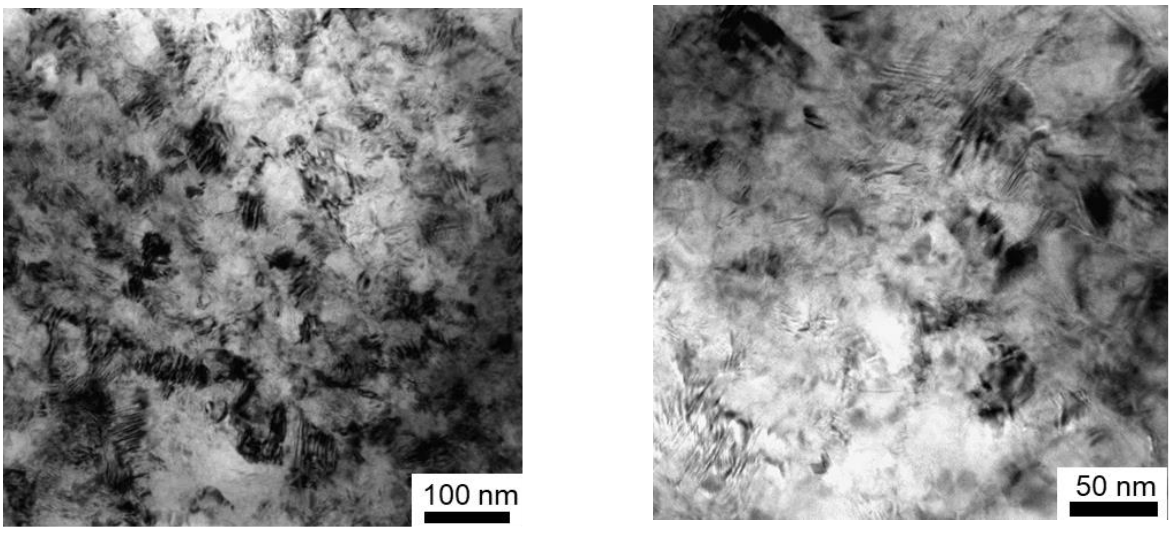

(a) (b)

Figure 4.4.2 TEM images of the 3D-printed CoCrFeNi alloy after HPT for (a) 1 turn and (b) 8 turns.

It is apparent that HPT processing refined the microstructure of the 3D-printed HEA significantly, so that the estimated average grain sizes are ~80 nm and ~60 nm after 1 and 8 turns by HPT. The observed micrographs demonstrate that the grains are reasonably equiaxed even after 1 HPT turn, and it was kept constant through 8 HPT turns. As was noted in the characterization section that the TEM observation was conducted at $r \approx 3.5$ mm, and it is reasonable to conclude that the microstructure was severely refined and saturated at $r \approx 3.5$ mm before 1 HPT turn. The result is fully consistent with the saturated Vickers microhardness value after 1 HPT turns at $r \approx 3.5$ mm, as shown in Figure 4.1.2. It should be noted that the observed ultrafine grain sizes of the 3D-printed HEA are in good agreement with ~61 ± 10 after 1 turns and 77 ± 10 nm after 10 turns for the as-cast HEA [42], and the consistency in grain size is resulted in the consistent values of saturated high hardness in these HEAs as was shown in Figures 4.1.1(a) and 4.1.2.

The as-cast CoCrFeNi alloy and HfNbTiZr alloys were characterized in our earlier collaboration work, and the refined microstructures after HPT for 1/4 and 5 for the CoCrFeNi alloy and 1 and 10 turns for the HfNbTiZr alloy are shown in Figures 4.4.3 (a) and (b) [46], and 4.4.4 (a) and (b), respectively [43]. An initial grain size of >20 μm was observed in the as-cast CoCrFeNi alloy. The microstructure was refined by HPT to have average grain sizes of ~77 ± 31 nm after 1/4 turn and ~45 ± 15 nm after 5 turns, where these values were directly measured using the TEM micrographs of Figure 4.4.3 (a) and (b).

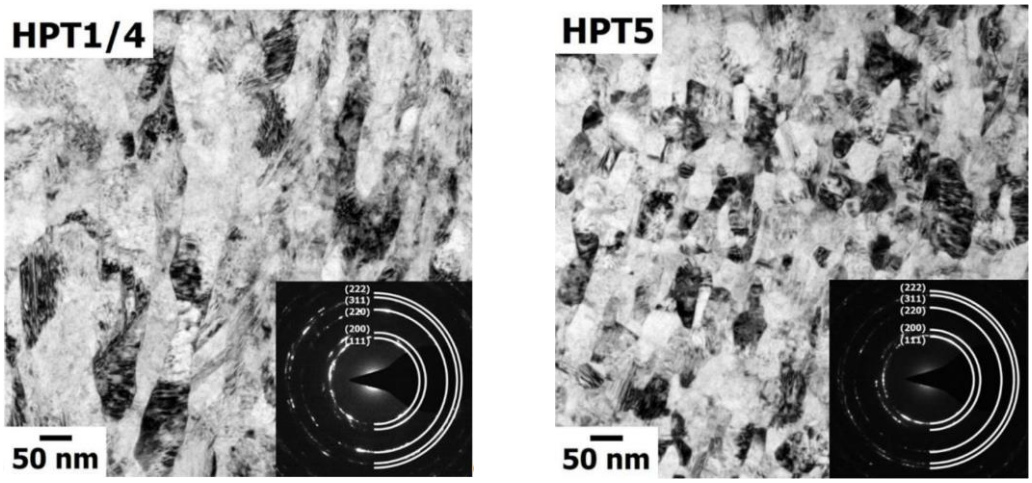

(a) (b)

Figure 4.4.3 TEM images of the as-cast CoCrFeNi *alloy after HPT for (a) 1/4 turn and (c) 5 turns [46].*

As was concluded in the hardness results, HPT for over 5 turns provide the saturated high hardness, and it is anticipated that HPT for 5 turns in the current study and 10 turns in Figure 4.4.3(b) can be reasonably consistent. In the report, an initial grain size of 13 μm in an as-cast condition was refined by HPT to have average grain sizes of 41 ± 6 nm after 1 turn and 31 ± 5 nm after10 turns, where these values were directly measured using the TEM micrographs of Figure 4.4.4 (a) and (b).

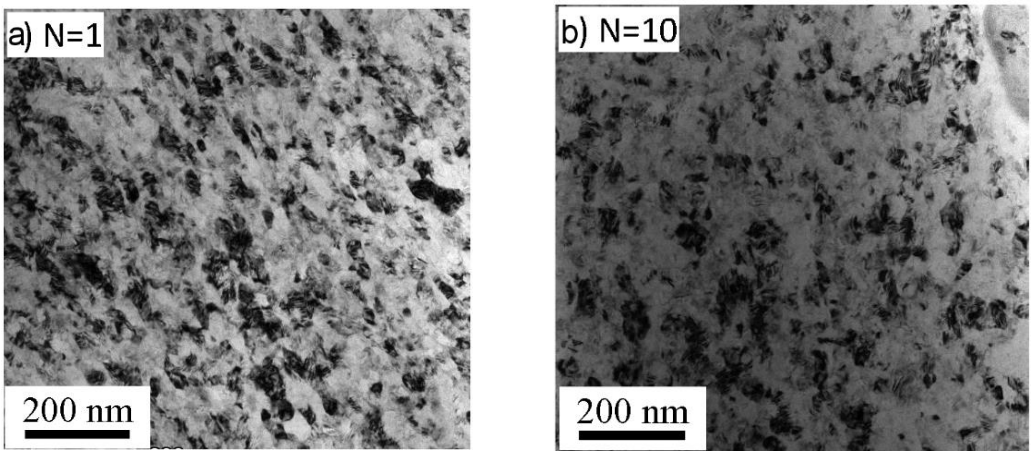

(a) (b)

Figure 4.4.4 TEM images of the as-cast HfNbTiZr alloy after HPT for (a) 1 turn and (c) 10 turns [43].

5 Discussion

5.1 Significant Hardness Evolution by HPT

It is well demonstrated that the hardness evolution towards high hardness through processing by HPT is mainly attributed to the severe grain refinement [47]. A hardness increase of polycrystalline materials can be well expressed by the Hall-Petch relationship, as shown in equation (1), and in an earlier report, the hardness increase was well validated by the Hall-Petch relationship for a CoCrFeNiMn HEA after HPT up to 2 turns [28]. Therefore, it is anticipated that the microstructural refinement is the major contribution to the hardness development towards the high values in the present three HEAs through HPT. Specifically, it was examined that the HPT straining enabled the activation of atomic diffusion in the CoCrFeNiMn HEA that resulted in the significant microstructural evolution [28], while HEAs are well known for its sluggish diffusion [48, 49].

The present results on hardness demonstrated the importance of increasing numbers of HPT turns, *N*. However, as was seen in equation (6) describing the estimation of equivalent strain introduced during HPT, the accumulated equivalent strain within a disk depends on the position. In order to understand the hardening behavior of the HEAs during HPT processing, it is indispensable to apply a different approach which considers the correlation between the recorded hardness values and the equivalent strain calculated using equation (6).

A plot of hardness versus equivalent strain is shown in Figure 5.1.1 for (a) as-cast CoCrFeNi alloy, (b) 3D-printed CoCrFeNi alloy, and (c) as-cast HfNbTiZr alloy after HPT processing under 6.0 GPa at room temperature. The values of equivalent strain were calculated by using the disk thickness, *h*, of 0.8 mm for all disks.

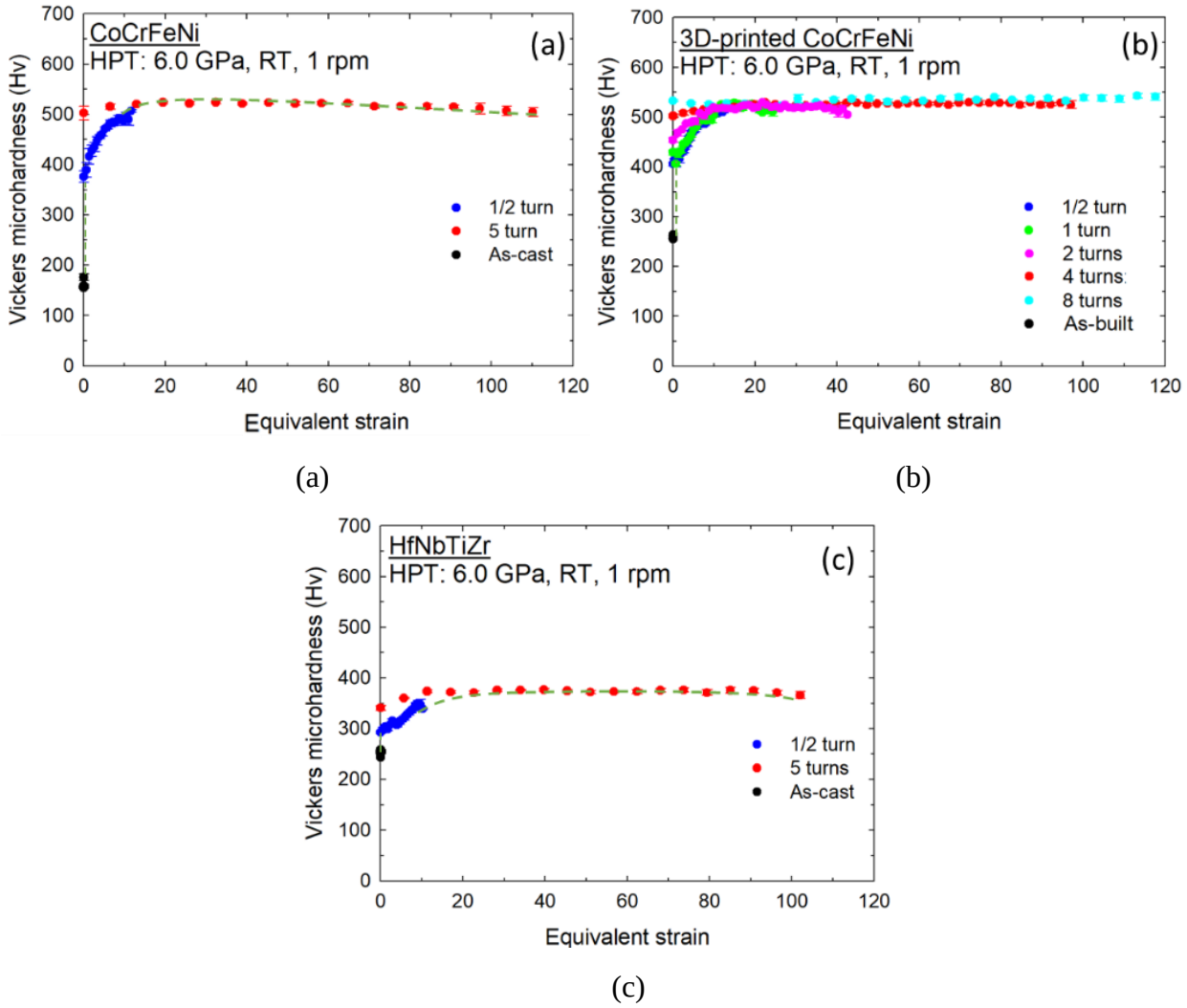

Figure 5.1.1 Vickers microhardness vs equivalent strain for (a) as-cast CoCrFeNi alloy, (b) 3D-printed CoCrFeNi alloy, and (c) as-cast HfNbTiZr alloy after processing by HPT.

The plots provide an important conclusion on the hardness developments in the HEAs. As was expected from the recorded hardness values in the earlier section, it is consistent for all HEAs that an accelerated hardness increase can be seen in an early stage of deformation, thus low equivalent strains up to ~12-15, which is followed by a saturated high hardness after continuous straining. This hardness behavior demonstrates the hardness model of strain hardening without recovery, and the hardness model was well defined in an earlier review report with additional two different hardness development models [50]. The schematic drawing of the

three separate hardness models are shown in Figure 5.1.3 for the HPT-processed materials showing (a) strain hardening without recovery, (b) strain hardening with recovery, and (c) strain softening with weakening [50].

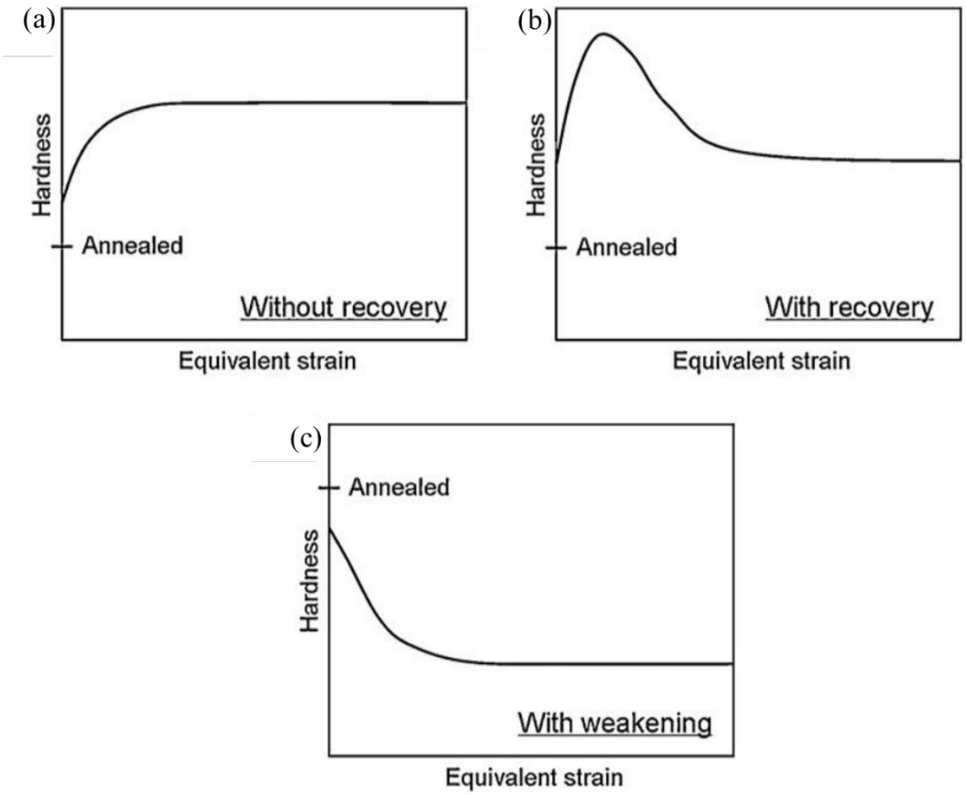

Figure 5.1.2 Schematic illustration of three types of variation of hardness with equivalent strain for metals processed by HPT: (a) hardening without recovery, for most metals, (b) hardening with recovery, (c) weakening. Typical levels for the initial annealed conditions are indicated [50].

Model (a) is for most metals and alloys, including HEAs where the materials increase hardness by straining and show the hardness saturation, while Model (b) shows the hardness increases initially, follows softening due to microstructural recovery, and saturate at the hardness higher than the initial hardness. The second model is often observed in highly pure metals having reasonably high melting temperature, T_m, such as Al, Mg, and Zn. The model (c) shows a very different hardness development with form two, where hardness dropped with straining and

saturated at the lower hardness in comparison with the initial hardness. This hardness model is observed in pure metals, which had lower T_m, such as Pb, Sn, and In. The review report specifically defined that the difference of the hardness development model can be defined by the homologous temperature of processing at room temperature, $298/T_m$ [50]. Since HEAs generally have high T_m, and thus the present three HEAs demonstrated the hardness evolution during HPT by the hardness development model of strain hardening without recovery.

It should be emphasized in Figure 5.1.1 that the equivalent strain of ~12-15 achieving the saturation of high hardness is consistent for all three HEAs, while these have different combinations of solute elements and atomic fractions as well as processing routes which cause different initial and final hardness values before and after HPT, respectively. In order to visualize the border strain for the hardness saturation, an additional display of the hardness versus equivalent strain in the double-natural logarithmic plots is useful, and the replotted double-logarithmic plots of the measured hardness against equivalent strain are shown in Figure 5.1.2 for (a) (a) as-cast CoCrFeNi alloy, (b) 3D-printed CoCrFeNi alloy, and (c) as-cast HfNbTiZr alloy after processing by HPT. The blue and red dotted trend lines describe the trend for the data at ε_{eq} >12 and <12, respectively, and the values of η represent the slopes of the trend lines in the double-natural logarithmic plots.

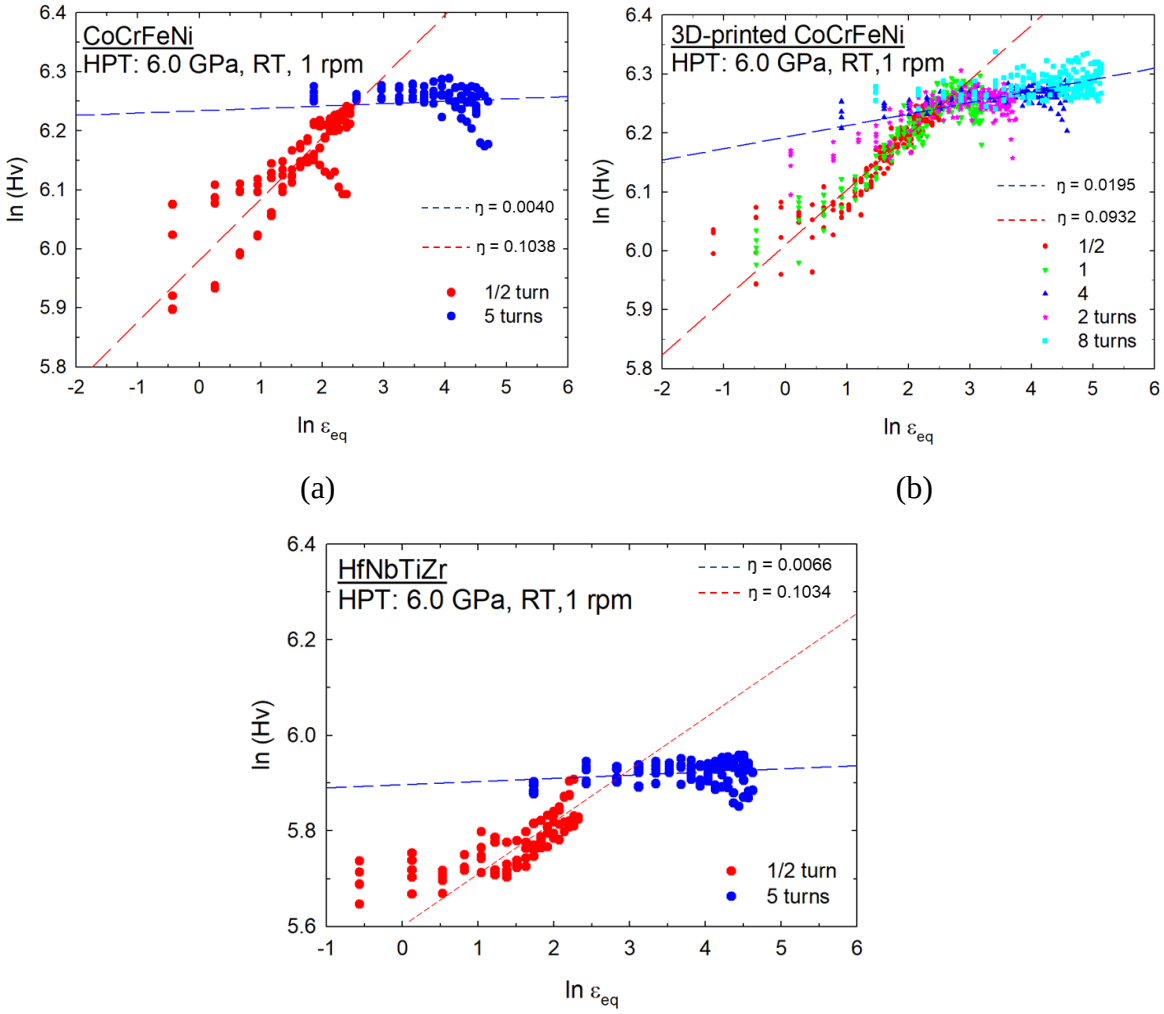

Figure 5.1.3 Double-natural logarithmic plots of Vickers microhardness vs equivalent strain for (a) as-cast CoCrFeNi alloy, (b) 3D-printed CoCrFeNi alloy, and (c) as-cast HfNbTiZr alloy after processing by HPT.

These plots demonstrate the hardness developments through HPT in the HEAs quantitatively. There are two clear stages of hardness development and the transition strains where the red trend dotted lines meet at the blue dotted trend lines are $\ln(\varepsilon_{eq}) \approx 2.5$, thus $\varepsilon_{eq} \approx$ 12-13 for all present HEAs. Thus, considering the plots shown in Figure 5.1.1, there is a significant hardness development up to $\varepsilon_{eq} \approx$ 12-13, and it is shown in the red dotted trend lines. These lines enable the quantitative expressions of the hardness evolution in the early stage of deformation with the following equations:

(a) $Hv \approx 395.44\varepsilon_{eq}^{0.1038}$ for the as-cast CoCrFeNi alloy after HPT.

(b) $Hv \approx 403.43\varepsilon_{eq}^{0.0932}$ for the 3D-printed CoCrFeNi alloy after HPT.

(c) $Hv \approx 275.11\varepsilon_{eq}^{0.1034}$ for the as-cast HfNbTiZr alloy after HPT.

The important value for evaluating the hardness development of materials during HPT can be the strain hardening exponent, η, which is the slope of the trend lines. Thus, the present HEAs are showing reasonably similar values of η = 0.0932-0.1038 for the CoCrFeNi alloys and η = 0.1034 for the HfNbTiZr alloy up to $\varepsilon_{eq} \approx$ 12-13. It is reasonable to note that a limited earlier reports demonstrates the strain hardening exponents of η = 0.08 for an AZ31 Mg alloy [51], η = 0.07 for a ZK60 Mg alloy [52], η = 0.031 for a Ti-6Al-4V alloy [53], and η = 0.017 for a Zn-3Mg alloy [54] after HPT for ε_{eq} <20 that is equivalent to $\ln(\varepsilon_{eq})$ <3. Thus, it is apparent from the comparison that the present HEAs demonstrate significantly high η, thereby exhibiting the high hardenability of these HEAs in an early stage of deformation by HPT.

Thereafter, the hardness development saturates at the high hardness values for each HEA at ε_{eq} >12-15 observed in the linear plots in Figure 5.1.1. However, the closer investigation of the hardness development in the logarithmic plots in Figure 5.1.3 allows the condensed vision of the hardness changes with equivalent strain. Specifically, the hardness increases slightly with increasing straining with η = 0.0040 and 0.0195 for the as-cast and the 3D-printed CoCrFeNi alloys, respectively, and η = 0.0066 for the as-cast HfNbTiZr alloy. It is interesting to note that the 3D-printed alloys show the highest strain hardening exponent than other as-cast HEAs at the highly deformed stage. It provides great potential of demonstrating better hardenability during plastic deformation, thus ductility and toughness. Such potential of improving ductility will be further evaluated in section 5.3 for the analysis of the nanoindentation results.

5.2 Bragg's Law and Williamson-Hall Analysis

The XRD line profiles for the 3D-printed CoCrFeNi alloy shown in Figure 4.2.1 reveal a simple f.c.c structure, and it is maintained consistent after processing by HPT. To better understand the structural changes from additive manufacturing to further HPT processing, the structure, lattice parameter, micro-strain, and crystallite size of the HEA are acquired by utilizing Bragg's law and Williamson-Hall analysis whose method assumes that a combination of crystallite size and strain contributes to the total breadth of a Bragg peak [55, 56].

The Bragg's law was used to calculate the lattice parameter in this study, based on the value of 2θ, where θ is the scattering angle. The equations are listed below,

$$n\lambda = 2d\sin(\theta) \tag{6}$$

$$d = \frac{a}{\sqrt{k^2+h^2+l^2}} \tag{7}$$

where n is the positive integer, usually taken as 1, λ is the wavelength of the X-ray source, d is the interplanar space, and h, k, l, are the miller indices. By using the equations (6) and (7), the lattice parameter of 0.3577 ± 0.0002 nm is estimated for the 3D-printed CoCrFeNi alloy before and after HPT, which is consistent with 0.3572 ± 0.0007 nm for the present as-cast CoCrFeNi alloy before and after HPT that was measured in our another collaborative research [42].

The Williamson-Hall method was used to calculate the micro-strain and the crystallite size in this study. In order to acquire these values, two types of strain should be considered as a part of the sample broadening, B_S, as shown in the equation (8),

$$B_s = B_L + B_\varepsilon \tag{8}$$

where B_L is the size broadening and B_ε is the strain broadening. The size broadening, B_L, is obtained by the Scherrer equation:

$$L = \frac{K\lambda}{B_L cos(\theta)} \quad (9)$$

where *L* is the average crystallite size, and *K* is a dimensionless shape factor, usually taken as 0.94 [57]. And, the strain broadening B_ε, is calculated from the equation below,

$$B_\varepsilon = 4\varepsilon\, tan(\theta) \quad (10)$$

where ε is the micro-strain. Thus, the equations (8), (9), and (10) allows of construction of a formula as follows:

$$B_s = \frac{K\lambda}{Lcos(\theta)} + 4\varepsilon\, tan(\theta) \quad (11)$$

Rearranging the equation (11) and substituting *K* with 0.94, the Williamson-Hall method yields,

$$B_s cos(\theta) = \frac{0.94\lambda}{L} + 4\varepsilon\, sin(\theta) \quad (12)$$

where B_s can be acquired with using the method of full width at half-maximum (FWHM) where there is an assumption that the grain size spreads homogeneously in reciprocal space. Thus, by plotting $B_s cos(\theta)$ vs 4 *sin(θ),* the crystallite size, *L*, can be obtained at the intercept of the regression line, and the micro-strain, ε, is estimated from the slope of the regression line.

The analyzed data are summarized in Table 1 showing the computed micro-strain and crystallite sizes for the initial CoCrFeNi alloy powders, as-built HEA sample before processing, and the HEA after HPT processing for 0.5-8 turns. For reference purposes, earlier results

showing crystallite size for the as-cast CoCrFeNi alloy after HPT for 1 and 10 turns that XRD line profile was shown in Figure 4.2.3(a) [42] are listed in Table 1 together.

Table 1. Micro-strain and crystallite size of the CoCrFeNi alloy obtained through the Williamson-Hall method.

CoCrFeNi		**Micro-strain, ε**	**Crystallite size, L** (nm)
3D-printed	Powder	0.001538	72.95225
	As-built	0.000633	45.22696
	HPT: 0.5 turn	0.001594	16.02019
	HPT: 1 turn	0.002573	18.18592
	HPT: 2 turns	0.002534	16.8341
	HPT: 4 turns	0.001879	15.14125
	HPT: 8 turns	0.00226	16.69008
As-cast [42]	HPT: 1 turn	-	30 ± 5
	HPT: 10 turns	-	28 ± 3

It is readily apparent in Table 1 that microstrain increased by HPT processing, and it yields very small crystallite sizes, while there is no significant increase in microstrain and reduction in the crystallite size with increasing numbers of HPT turns. The actual grain size is expected to be slightly larger than the crystallite size measured by the method using the XRD data, as described earlier [58]. Thus, the crystallite sizes after 1 and 8 turns are ~18.2 and 16.7 nm, respectively, in Table 1, while the TEM micrographs provided grain sizes of ~80 and 60 nm in Figure 4.4.2 for the HEA alloys after 1 and 8 HPT turns, respectively. This phenomenon is often observed in a usual phenomenon in SPD-processed materials involving a hierarchical microstructure, where the grains are fragmented into subgrains and dislocation cells [42]. Nevertheless, this significant grain refinement in the HEA by HPT is anticipated to provide a major contribution to such high hardness observed in this study.

Different manufacturing processes of casting and additive manufacturing introduced a difference in the crystallite size after HPT, while as was mentioned in section 4.4 that the grain

sizes of these alloys measured directly from the TEM micrographs are consistent. The smaller crystallite size implies a higher population of subgrain boundaries due to the presence of pre-strain, thus pre-microstrain, for the production of the HEAs powders and during the building process before HPT processing in comparison with the as-cast material, which has a fully solutionized condition without any pre-straining.

5.3 Plasticity and Deformation Mechanism

The load-displacement curves obtained through nanoindentation are used to analyze two important characteristics of the HEA materials, strain rate sensitivity, *m*, and the activation volume, *V**. Specifically, strain rate sensitivity implies plasticity, thus the potential of ductility, and the activation volume suggests a possible dominant deformation mechanism.

The strain rate sensitivity, *m*, can be determined, at a given strain, ε, and absolute temperature, *T*, by considering Tabor's empirical prediction, by the flow stress, σ_f, which is equivalent to *H*/3 for fully plastic deformation at a constant strain rate $\dot{\varepsilon}$ [59], where *H* is the nanoindentation hardness estimated according to the Oliver-Pharr method [60],

$$m = \left(\frac{\partial \ln \sigma_f}{\partial \ln \dot{\varepsilon}}\right)_{\varepsilon,T} = \left(\frac{\partial \ln(H/3)}{\partial \ln \dot{\varepsilon}}\right)_{\varepsilon,T} \quad (13)$$

Thus, the values of *m* can be computed from the slopes of the lines in a logarithmic plot of *H*/3 against $\dot{\varepsilon}$ as shown in Figure 5.3.1 for (a) the as-built CoCrFeNi alloy, (b) the 3D-printed CoCrFeNi alloy after HPT for 8 turns, and (c) the as-cast CoCrFeNi for 5 HPT turns.

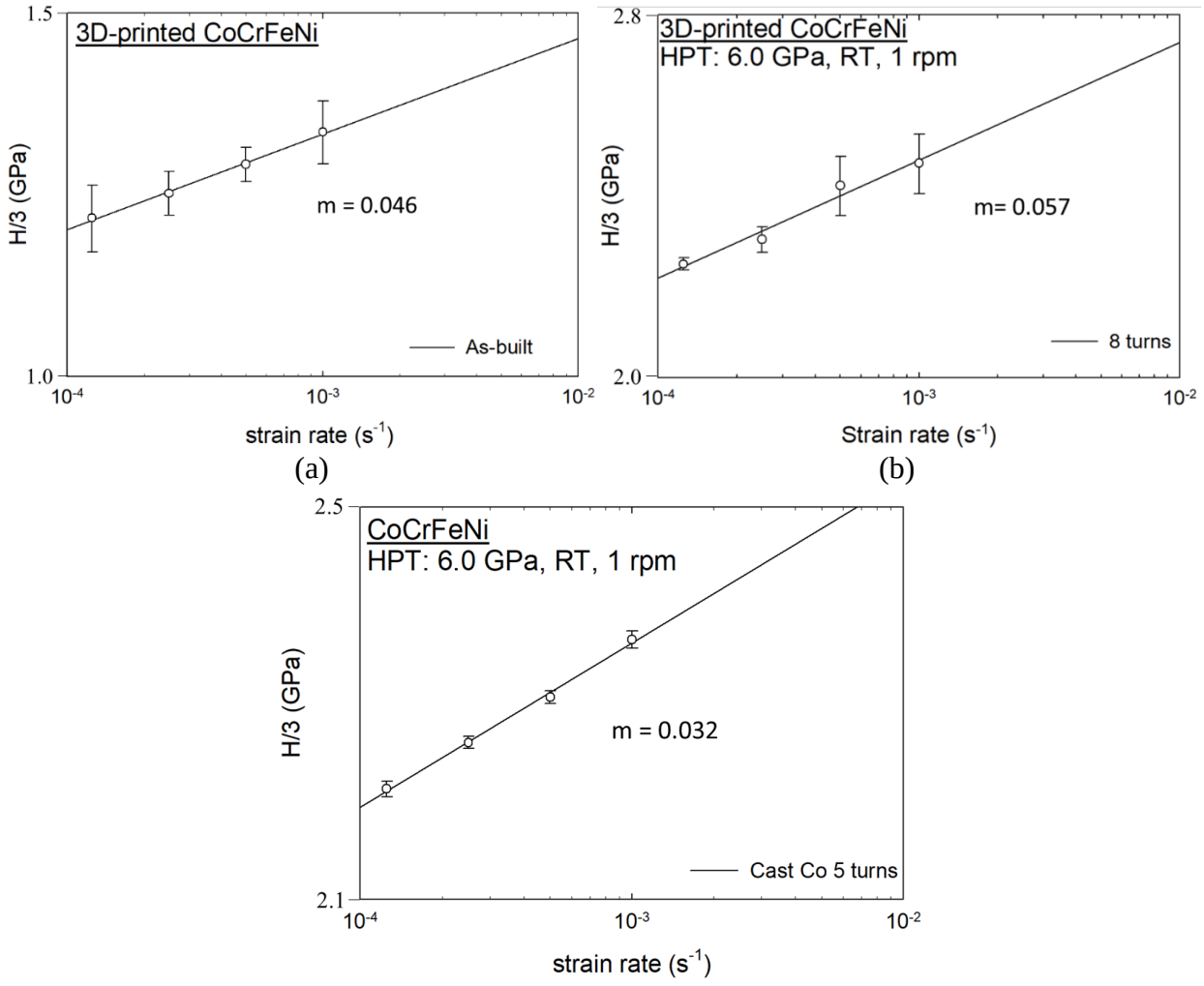

Figure 5.3.1 Logarithmic plots of H/3 vs strain rate for (a) the as-built CoCrFeNi alloy, (b) the 3D-printed CoCrFeNi alloy after HPT for 8 turns, and (c) the as-cast CoCrFeNi for 5 HPT turns.

The *m* values for the as-built CoCrFeNi alloy, the 3D-printed CoCrFeNi alloy after HPT for 8 turns, and the as-cast CoCrFeNi alloy after 5 HPT turns are estimated as 0.046, 0.057 and 0.032, respectively. These *m* values obtained for the CoCrFeNi alloys before and after HPT are reasonably similar to the *m* values of ~0.038 and ~0.031 observed for an as-cast CoCrFeNiMn alloy before and after HPT up to 2 turns, respectively [28]. Closer observation with the reference *m* values shows that the as-cast HEA shows a decreased m value after grain refinement, thus reduction in plasticity, while the 3D-printed HEA improves plasticity by increasing the m value

with even increasing its hardness and strength as shown in Section 4.1. The reason may be related to the manufacturing technique, and it requires further experiments to identify the reasons. Nevertheless, the improved strain rate sensitivity as well as the improved degree of strain hardening (see Section 5.1) imply the significant potential of demonstrating high ductility in the 3D-printed HEA after grain refinement via HPT, while the material has excellent hardness and strength.

It is also reasonable to note that general coarse-grained f.c.c metals, such as pure Ni showing $m \approx 0.0028$ [61], the present as-built HEA alloy before HPT showing $m \approx 0.046$ in Figure 5.3.1(a) and the present as-cast HEA showing $m \approx 0.038$ [28] demonstrate over one order of magnitude higher m value. These general f.c.c metals increases strain rate sensitivity with grain refinement by SPD [1], e.g. $m \approx 0.015$–0.034 for nanocrystalline Ni having $d < 100$ nm [29, 62, 63, 64]. Thus, the HEAs maintain plasticity without significant reduction, or even increase slightly, with grain refinement through HPT, while their hardness and strength are significantly improved by processing.

For further discussion on the *m* values for similar HEAs, Figure 5.3.2 shows a plot of the strain rate sensitivity, *m*, against grain size, *d*, for various Co-based HEAs [48, 65-74]. The materials having ultrafine grain sizes of ~5–100 nm are within a red square, while coarse-grained HEAs having grain sizes of ~4–200 μm are within a gray squire. The present as-cast CoCrFeNi alloy after 5 HPT turns, the as-built CoCrFeNi alloy without processing and after processing for 8 turns are listed in the plot with their crystallite size shown in Table 1.

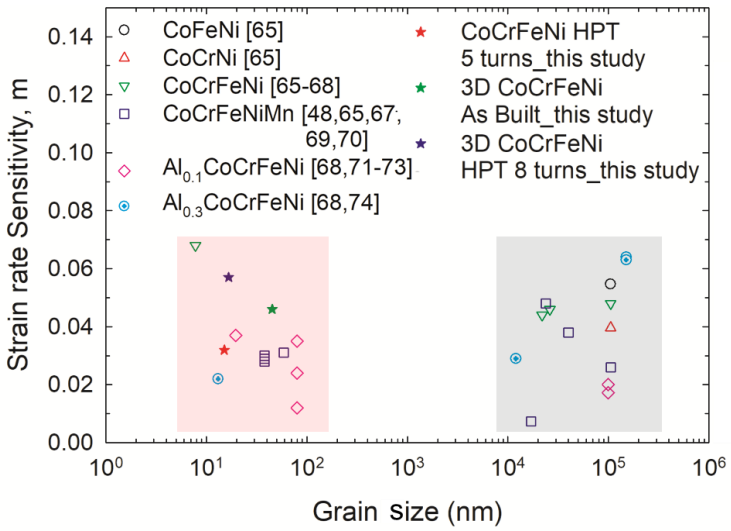

Figure 5.3.2 Strain rate sensitivity, m, vs grain size, d, for various Co-based f.c.c HEAs [48, 65-74].

The present results on the as-cast and 3D-printed CoCrFeNi alloys show reasonably high *m* value in the nanocrystalline grain sizes compare to the other nano-grained HEAs as well as the coarse-grained HEAs. The plot implies that the Co-based HEAs having an f.c.c structure can demonstrate desirable plasticity in a wide range of grain sizes towards a nanocrystalline range. This confirms the feasibility of grain refinement through HPT for achieving both high strength and ductility in the Co-based f.c.c HEAs.

It should be noted that, although the present HfNbTiZr alloy having a b.c.c structure (see Figure 4.2.3(b)) was not tested by nanoindentation, it is reported earlier that b.c.c materials often fail to show the trend of increasing m value with grain size reduction [75], while there is at present less information to conclude the trend for the b.c.c metals processed by SPD. Nevertheless, grain refinement by utilizing HPT is an excellent strategy for improving both strength and ductility in UFG f.c.c. HEAs by enhancing both strain hardening and strain rate sensitivity.

To understand the dominant deformation mechanisms of the HEAs, the activation volume, V^*, is calculated in this study by using the equation (14).

$$V^* = \sqrt{3}kT\left(\frac{\partial ln\ \dot{\varepsilon}}{\partial(H/3)}\right) = \frac{3\sqrt{3}kT}{mH} \quad (14)$$

where *k* is Boltzmann's constant, *T* is the absolute temperature. Thus, using Equation (14), the value of V_p^* was determined from the slope of a trend linear of natural logarithmic strain rate versus linear flow stress for each sample. The estimated V^* values for the materials in this study are shown in Table 2, where *b* is the Burgers vector, where Burgers vector for the alloys were calculated by $b = a \times \sqrt{2}/2 \approx 2.52 \times 10^{-10}m$ where *a* is the lattice parameter of 3.57 Å. The as-cast CoCrFeNi alloy before HPT was tested in an earlier collaborative study and the estimated *V** value was listed in Table 2 together.

Table 2 Activation volume for the Co-based HEAs.

Material	Activation volume × b^3, V^* (m^3)
As-built 3D-printed CoCrFeNi alloy	7.64 b^3
3D-printed CoCrFeNi alloy, HPT for 8 turns	3.20 b^3
As-cast CoCrFeNi alloy without HPT [46]	~20 b^3
As-cast CoCrFeNi alloy, HPT for 5 turns	6.12 b^3

It was defined in an earlier report that the value of V^* can estimates the dominant deformation mechanism of the materials [64], where ~100b^3 to ~1000b^3 for dislocation glide of f.c.c metals [76], ~10b^3 for grain boundary sliding [77], and an enhanced short-range barrier to dislocation motion in f.c.c HEAs [65], and ~1b^3 for diffusion either along the grain boundary or through lattice [77,78]. The as-built CoCrFeNi alloy shows a value of 7.64b^3 m^3 before processing and HPT processing reduces to 3.20b^3 m^3. Both are smaller than ~10 b^3 suggesting that its deformation mechanism follows conventional nanocrystalline metals, i.e. grain boundary-mediated dislocation activities. As was noted in section 4.4, the as-cast CoCrFeNi alloy had a

coarse grain size with >20 μm and it is resulted in the activation volume of ~20 b^3 m^3 [46] denoting the enhanced short-range barriers, e.g. Peierls barriers and/or chemical short-range barrier, to dislocation motion. Processing by HPT for 5 turns reduced the activation volume to 6.12 b^3 and the predominant deformation mechanism of the as-cast alloy was transformed into grain boundary-mediated dislocation activity with grain refinement.

In order to analyze a tendency of the deformation mechanism for the f.c.c HEAs with grain refinement, Figure 5.3.3 shows the plot of the activation volume against grain size for several Co-based f.c.c HEAs [48, 65, 66, 68-72]. In the same way in Figure 5.3.2, the materials having ultrafine grain sizes of ~5–100 nm are within a red square, while coarse-grained HEAs having grain sizes of ~4–200 μm are within a gray square.

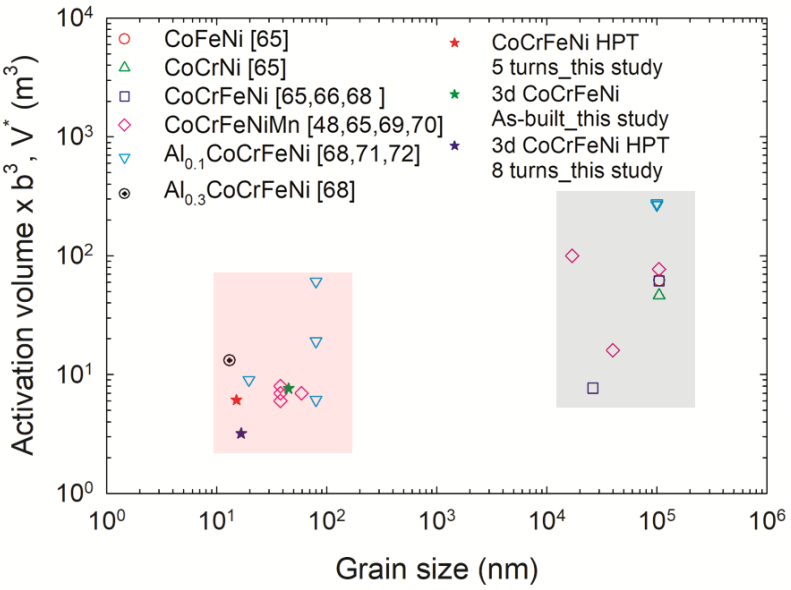

Figure 5.3.3 Activation volume against grain size for various Co-based f.c.c HEAs [48, 65, 66, 68-72].

It is visualized by the plot that there is a general tendency that the activation volume maintains the same or even decreases with grain refinement in the f.c.c HEAs. Although there are some

exceptions, with no dependency on the manufacturing process, most f.c.c HEAs, including the present HEAs, tend to demonstrate the consistent deformation mechanism of grain boundary-mediated dislocation activity after grain refinement.

6 Summary and Conclusion

1) The significant hardness evolution was observed after HPT processing for HEAs from 160 hv to 525 hv for an as-cast CoCrFeNi HEA, 250 hv to 375 hv for an as-cast HfNbTiZr HEA, and 250 hv to 525 hv for a 3D-printed CoCrFeNi HEA.

2) With the consistent composition, materials processed by different routes show different initial hardness values but reach to the consistent saturated hardness values of 525 hv after HPT processing for high numbers of turn. The different hardness before HPT processing is attributed to the initial microstructural conditions.

3) Microstructural analysis demonstrated all HEAs in the present study show homogeneous microstructure with equiaxed ultrafine-grains after 5 or more numbers of HPT turns under 6.0 GPa.

4) In an early stage of deformation up to an equivalent strain smaller than 12 by HPT, the HEAs exhibit a high strain hardening exponent value, which indicates a high hardenability compared to conventional metallic alloys.

5) XRD analysis using the Williamson-hall method demonstrated the significant structural refinement in the 3D-printed CoCrFeNi HEA by HPT processing. The computed crystallite size decreased from 45.2 nm for the as-built sample to 16 nm for the sample after HPT processing.

6) Both CoCrFeNi HEAs demonstrated improved strain rate sensitivity by grain refinement though HPT, and these are comparable or even higher in comparison with conventional f.c.c. metals and alloys. The 3D-printed HEA after HPT demonstrated higher strain rate sensitivity,

thus plasticity, as well as higher strain hardening ratio than the cast HEA. It implies that there is a great optional of showing excellent ductility in the 3D-printed CoCrFeNi HEA.

7) The activation volume values before and after HPT processing are smaller than 10 b^3 for the 3D-printed CoCrFeNi HEA, thereby indicating the conventional nanocrystalline metal deformation mechanism of grain boundary-mediated dislocation activities.

7 Future work

1. Structural stability of ultrafine-grained HEAs at high temperature.

Significant microstructure evolution was introduced in HEAs by HPT processing in this study. However, since grain refinement introduced by HPT is metastable and the time-dependent recovery was reported in many earlier reports. Thus, it is worthwhile to analyze the structural stability of the HPT-processed HEAs at elevated temperatures. The materials will be put in the Differential Scanning Calorimetry (DSC) facility, to reveal the recovery and recrystallization temperature. The result will be correlated with the results from XRD analysis, hardness testing, to analyze the structural and hardness changes with temperature.

2. Influence of different manufacturing procedures on structure and mechanical properties of HEAs.

Figure 7.1.1 is the double logarithmic plot of H/3 vs strain rate for four different HEA samples.

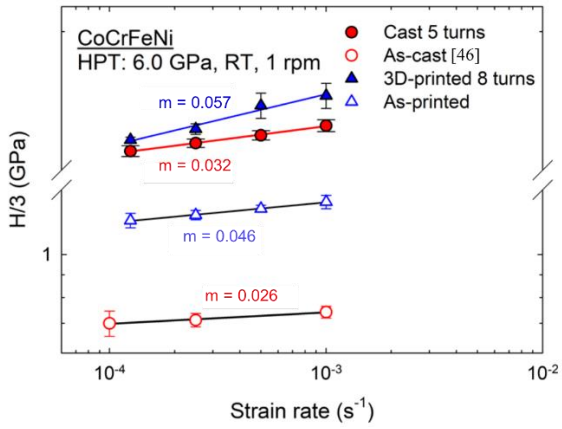

Figure 7.1.1 Double logarithmic plot of H/3 vs strain rate for as-cast CoCrFeNi HEA, as-cast CoCrFeNi HEA 5 turns, 3D-printed CoCrFeNi HEA 8 turns, As-built CoCrFeNi HEA

The Vickers microhardness of the HPT-processed CoCrFeNi alloys are consistent, but both the strain hardening rate and the strain rate sensitivity were higher in the 3D-printed HEA. This different response could be caused by their different manufacturing procedures. This may be anticipated by the fact that 3D-printed techniques involve powders having high pre-strain, which may affect to introduce an ultimate fraction of high-angle grain boundaries after grain refinement. In order to analyze the possible reasons, better understanding of structural and microstructural changes is required after grain refinement. The analysis will require a series of characterization techniques such as TEM, nanoindentation test, and XRD.

3. Miniature tensile testing for bulk scale mechanical properties

Due to the sample size limitation, the conventional tensile test cannot be applied to the HPT-processed HEAs. The miniature tensile tests are developed to analyze the stress-strain responses in bulk scale by the miniature sample (as shown in Figure 2.3.5) in comparison with the sample volume used in nanoindentation and Vickers microhardness. Moreover, the values of strain rate sensitivity obtained in the miniature tensile testing can be compared with those from nanoindentation.

Bibliography

[1] M. Kawasaki, B. Ahn, P. Kumar, J.-i. Jang, T.G. Langdon, Nano- and micro-mechanical properties of ultrafine-grained materials processed by severe plastic deformation techniques. Adv. Eng. Mater., 19(1) (2017) 1600578.

[2] E. Ma, Eight routes to improve the tensile ductility of bulk nanostructured metals and alloys. JOM 58 (2006) 49.

[3] E. Ma, Instabilities and ductility of nanocrystalline and ultrafine-grained metals. Scr. Mater., 49(7) (2003) 663.

[4] E.O. Hall, The deformation and ageing of mild steel: III discussion of results. Proc. Phys. Soc., B, 64(9) (1951) 747.

[5] N.J. Petch, The cleavage strength of polycrystals. J Iron Steel Inst, 174 (1953) 25.

[6] T. Mungole, K. Praveen, M. Kawasaki, T.G. Langdon, A critical examination of the paradox of strength and ductility in ultrafine-grained metals. J. Mater. Res, 29(21) (2014) 2534.

[7] P.W. Bridgman. The effect of hydrostatic pressure on plastic flow under shearing stress. J. Appl. Phys. 17 (1946) 692.

[8] R.Z. Valiev, I.V. Alexandrov, Y.T. Zhu, T.C. Lowe, Paradox of strength and ductility in metals processed by severe plastic deformation. J. Mater. Res, 17(1) (2002) 5

[9] N. Balasubramanian, T.G. Langdon, The strength–grain size relationship in ultrafine-grained metals. Metall Mater Trans A, 47A (2016) 5827.

[10] A.P. Zhilyaev, T.G. Langdon, Using high-pressure torsion for metal processing: Fundamentals and applications. Prog. Mater. Sci, 53(6) (2008) 893.

[11] R.Z. Valiev, T.G. Langdon, Principles of equal-channel angular pressing as a processing tool for grain refinement. Prog. Mater. Sci, 51(7) (2006) 881.

[12] R.Z. Valiev, R.K. Islamgaliev, I.V. Alexandrov, Bulk nanostructured materials from severe plastic deformation. Prog. Mater. Sci., 45(2) (2000) 103.

[13] P.W. Bridgman. On torsion combined with compression. J. Appl. Phys., 14, (1943) 273.

[14] R.Z. Valiev, Y. Estrin, Z. Horita, T.G. Langdon, M.J. Zechetbauer, Y.T Zhu, Producing bulk ultrafine-grained materials by severe plastic deformation. JOM 58(4) (2006) 33.

[15] Y. Estrin, A.Vinogradov, Extreme grain refinement by severe plastic deformation: A wealth of challenging science. Acta Mater, 61(3) (2013) 782.

[16] Y. Iwahashi, J. Wang, Z. Horita, M. Nemoto, T.G. Langdon, Principle of equal-channel angular pressing for the processing of ultra-fine grained materials. Scr. Mater, 35(2) (1996) 143.

[17] M. Kawasaki, T.G. Langdon, Flow behavior of a superplastic Zn–22% Al alloy processed by equal-channel angular pressing. Mater. Sci. Eng. A, 503(1) (2009) 48.

[18] Y. Saito, H. Utsunomiya, N. Tsuji, T. Sakai, Novel ultra-high straining process for bulk materials—development of the accumulative roll-bonding (ARB) process. Acta Mater, 47(2) (1999) 579

[19] D. Yang, P. Cizek, P. Hodgson, C. Wen, Ultrafine equiaxed-grain Ti/Al composite produced by accumulative roll bonding. Scr. Mater, 62(5) (2010) 321.

[20] N. Thangapandian, S. Balasivanandha Prabu, K.A. Padmanabhan, Effects of die profile on grain refinement in Al–Mg alloy processed by repetitive corrugation and straightening. Mater. Sci. Eng. A, 649 (2016) 229.

[21] J.Y. Huang, Y.T. Zhu, H. Jiang, T.C. Lowe, Microstructures and dislocation configurations in nanostructured Cu processed by repetitive corrugation and straightening. Acta Mater., 49(9) (2001) 1497.

[22] C. Xu, Z. Horita, T.G. Langdon, The evolution of homogeneity in an aluminum alloy processed using high-pressure torsion. Acta Mater., 56(18) (2008) 5168.

[23] A.P. Zhilyaev, T.R. McNelley, T.G. Langdon, Evolution of microstructure and microtexture in fcc metals during high-pressure torsion. J. Mater. Sci., 42(5) (2007) 1517.

[24] R.Z. Valiev, Yu.V. Ivanisenko, E.F. Rauch, B. Baudelet, Structure and deformaton behaviour of Armco iron subjected to severe plastic deformation. Acta Mater., 44(12) (1996) 4705.

[25] J. Wongsa-Ngam, M. Kawasaki, Y. Zhao, T.G. Langdon, Microstructural evolution and mechanical properties of a Cu–Zr alloy processed by high-pressure torsion. Mater. Sci. Eng. A, 528(25-26) (2011) 7715.

[26] Y. Estrin, A. Molotnikov, C.H.J. Davies, R. Lapovok, Strain gradient plasticity modelling of high-pressure torsion. J Mech Phys Solids, 56(4) (2008) 1186.

[27] G. Sakai, Z. Horita, T.G. Langdon, Grain refinement and superplasticity in an aluminum alloy processed by high-pressure torsion. Mater. Sci. Eng. A, 393(1-2) (2005) 344.

[28] D.-H. Lee, I.-C. Choi, M.-Y. Seok, J. He, Z. Lu, J.-Y. Suh, M. Kawasaki, T.G. Langdon, J.-i. Jang, Nanomechanical behavior and structural stability of a nanocrystalline CoCrFeNiMn high-entropy alloy processed by high-pressure torsion. J. Mater. Res., 30(18) (2015) 2804.

[29] R. Schwaiger, B. Moser, M. Dao, N. Chollacoop, S. Suresh, Some critical experiments on the strain-rate sensitivity of nanocrystalline nickel. Acta Mater., 51(17) (2003) 5159.

[30] J.-W. Yeh, S.-K. Chen, S.-J Lin, J.-Y. Gan, T.-S. Chin, T.-T. Shun, C.-H. Tsau, S.-Y. Chang, Nanostructured high-entropy alloys with multiple principal elements: Novel alloy design concepts and outcomes. Adv. Eng. Mater., 6(5) (2004) 299.

[31] Y. Kuzminova, D. Firsov, A. Dudin, S. Sergeev, A. Zhilyaev, A. Dyakov, A. Chupeeva, A. Alekseev, D. Martynov, I. Akhatov, S. Evlashin, The effect of the parameters of the powder bed fusion process on the microstructure and mechanical properties of CrFeCoNi medium-entropy alloys. Intermetallics, 116 (2020) 106651.

[32] Y. Zhang, S.G. Ma, J.W. Qiao, Morphology transition from dendrites to equiaxed grains for AlCoCrFeNi high-entropy alloys by copper mold casting and bridgman solidification. Metall Mater Trans A Phys Metall Mater Sci, 43(8) (2011) 2625.

[33] L.M. Wang, C.C. Chen, J.W. Yeh, S.T. Ke, The microstructure and strengthening mechanism of thermal spray coating Ni x Co 0.6Fe 0.2Cr y Si z AlTi 0.2 high-entropy alloys. Mater. Chem. Phys., 126(3) (2011) 880.

[34] X.F. Wang, Y. Zhang, Y. Qiao, G.L. Chen, Novel microstructure and properties of multicomponent CoCrCuFeNiTi x alloys. Intermetallics, 15(3) (2007) 357.

[35] Y.J. Zhou, Y. Zhang, Y.L. Wang, G.L. Chen, Solid solution alloys of Al Co Cr Fe Ni Ti x with excellent room-temperature mechanical properties. Appl. Phys. Lett., 90(18) (2007) 181904.

[36] F. Otto, A. Dlouhý, Ch. Somsen, H. Bei, G. Eggeler, E.P. George, The influences of temperature and microstructure on the tensile properties of a CoCrFeMnNi high-entropy alloy. Acta Mater., 61(15) (2013) 5743.

[37] W. Ji, W. Wang, H. Wang, J. Zhang, Y. Wang, F. Zhang, Z. Fu, Alloying behavior and novel properties of CoCrFeNiMn high-entropy alloy fabricated by mechanical alloying and spark plasma sintering. Intermetallics, 56 (2015) 24.

[38] Y.D. Wu, Y.H. Cai, T. Wang, J.J. Si, J. Zhu, Y.D. Wang, X.D. Hui, A refractory Hf25Nb25Ti25Zr25 high-entropy alloy with excellent structural stability and tensile properties. Mater. Lett., 130 (2014) 277.

[39] C.-M. Lin, C.-C. Juan, C.-H. Chang, C.-W. Tsai, J.-W. Yeh, Effect of Al addition on mechanical properties and microstructure of refractory AlxHfNbTaTiZr alloys. J. Alloys Compd., 624 (2015) 100.

[40] S.J. Sun, Y.Z. Tian, H.R. Lin, X.G. Dong, Y.H. Wang, Z.J. Zhang, Z.F. Zhang, Enhanced strength and ductility of bulk CoCrFeMnNi high entropy alloy having fully recrystallized ultrafine-grained structure. Mater. Des., 133 (2017) 122.

[41] L. Lutterotti, S. Matthies, H.R. Wenk. (1999). MAUD (Material Analysis Using Diffraction): a user friendly Java program for Rietveld texture analysis and more, Proceeding of the twelfth international conference on textures of materials (ICOTOM-12), NRC Research Press, Ottawa, Canada, pp. 1599-1604.

[42] J. Gubicza, P.T. Hung, M. Kawasaki, J.-K. Han, Y. Zhao, Y. Xue, J.L. Lábár, Influence of severe plastic deformation on the microstructure and hardness of a CoCrFeNi high-entropy alloy: A comparison with CoCrFeNiMn. Mater. Charact., 154 (2019) 304.

[43] J. Gubicza, A. Heczel, M. Kawasaki, J.-K. Han, Y. Zhao, Y. Xue, S. Huang, J.L. Lábár, Evolution of microstructure and hardness in Hf25Nb25Ti25Zr25 high-entropy alloy during high-pressure torsion. J. Alloys Compd., 788 (2019) 318.

[44] J.-K. Han, K.-D. Liss, T.G. Langdon, M. Kawasaki, Synthesis of a bulk nanostructured metastable Al alloy with extreme supersaturation of Mg. Sci. Rep., 9(1) (2019) 17186.

[45] C.L. Wang, Y.H. Lai, J.C. Huang, T.G. Nieh, Creep of nanocrystalline nickel: A direct comparison between uniaxial and nanoindentation creep. Scr. Mater, 62(4) (2010) 175.

[46] Y. Zhao, X. Wang, T. Cao, J.-K. Han, M. Kawasaki, J.-i. Jang, H.N. Han, U. Ramamurty, L. Wang, Y. Xue, Effect of grain size on the strain rate sensitivity of CoCrFeNi high-entropy alloy. Mater. Sci. Eng. A, 782 (2020) 139281.

[47] T.G. Langdon, Twenty-five years of ultrafine-grained materials: Achieving exceptional properties through grain refinement. Acta Mater, 61(19) (2013) 7035

[48] Y. Zhang, T. T. Zuo, Z. Tang, M.C. Gao, K.A. Dahmen, P.K. Liaw, Z.P. Lu, Microstructures and properties of high-entropy alloys. Prog. Mater. Sci., 61 (2014) 1.

[49] B.S. Murty, J.W. Yeh, S. Ranganathan, High-entropy alloys. Elsevier: Butterworth-heinemann.

[50] M. Kawasaki, B. Ahn, T.G. Langdon, Significance of strain reversals in a two-phase alloy processed by high-pressure torsion. Mater. Sci. Eng. A, 527(26) (2010) 7008.

[51] M. Kawasaki, R.B. Figueiredo, Y. Huang, T.G. Langdon, Interpretation of hardness evolution in metals processed by high-pressure torsion. J. Mater. Sci., 49(19), (2014). 6586.

[52] S.A. Torbati-Sarraf, S. Sabbaghianrad, R.B. Figueiredo, T.G. Langdon, Orientation imaging microscopy and microhardness in a ZK60 magnesium alloy processed by high-pressure torsion. J. Alloys Compd., 712 (2017) 185.

[53] Y.C. Wang, T.G. Langdon, Effect of heat treatment on microstructure and microhardness evolution in a Ti–6Al–4V alloy processed by high-pressure torsion. J. Mater. Sci., 48(13), (2013) 4646.

[54] D. Hernández-Escobar, J. Marcus, J.-K. Han, R.R. Unocic, M. Kawasaki, C.J. Boehlert, Effect of post-deformation annealing on the microstructure and micro-mechanical behavior of Zn–Mg hybrids processed by high-pressure torsion. Mater. Sci. Eng. A, 771, (2020) 138578.

[55] G.K. Williamson, W.H. Hall, X-ray line broadening from filed aluminum and wolfram. Acta Metall. Mater., 1(1), (1953) 22.

[56] E.J. Mittemeijer, U. Welzel, The “state of the art” of the diffraction analysis of crystallite size and lattice strain. Z. Kristallog., 223(9) (2008) 552.

[57] A.L. Patterson, The scherrer formula for X-ray particle size determination. Phys. Rev., 56(10) (1939) 978.

[58] A. Heczel, M. Kawasaki, J.L. Lábár, J.-i. Jang, T.G. Langdon, J. Gubicza, Defect structure and hardness in nanocrystalline CoCrFeMnNi high-entropy alloy processed by high-pressure torsion. J. Alloys Compd., 711 (2017) 143.

[59] S. Shim, J.-i. Jang, G.M. Pharr, Extraction of flow properties of single-crystal silicon carbide by nanoindentation and finite-element simulation. Acta Mater., 56(15) (2008) 3824.

[60] W.C. Oliver, G.M. Pharr, An improved technique for determining hardness and elastic modulus using load and displacement sensing indentation experiments. J. Mater. Res., 7(6) (1992) 1564.

[61] F. Dalla Torre, P. Spätig, R. Schäublin, M. Victoria, Deformation behavior and microstructure of nanocrystalline electrodeposited and high pressure torsioned nickel. Acta Mater., 53(8) (2005) 2337.

[62] Q. Wei, S. Cheng, K.T. Ramesh, E. Ma, Effect of nanocrystalline and ultrafine grain sizes on the strain rate sensitivity and activation volume: fcc versus bcc metals. Mater. Sci. Eng. A, 381(1-2) (2004) 71.

[63] J. Chen, L. Lu, K. Lu, Hardness and strain rate sensitivity of nanocrystalline Cu. Scr. Mater, 54(11) (2006) 1913

[64] Y. Wang, A. Hamza, E. Ma, Temperature-dependent strain rate sensitivity and activation volume of nanocrystalline Ni. Acta Mater., 54(10) (2006) 2715.

[65] Z. Wu, Y. Gao, H. Bei, Thermal activation mechanisms and Labusch-type strengthening analysis for a family of high-entropy and equiatomic solid-solution alloys. Acta Mater., 120(C) (2016) 108.

[66] W. Huo, F. Fang, X. Liu, S. Tan, Z. Xie, J. Jiang, Remarkable strain-rate sensitivity of nanotwinned CoCrFeNi alloys. Appl. Phys. Lett., 114(10), (2019) 101904.

[67] M. Shabani, J. Indeck, K. Hazeli, P.D. Jablonski, G.J. Pataky, Effect of strain rate on the tensile behavior of CoCrFeNi and CoCrFeMnNi high-entropy alloys. J. Mater. Eng. Perform., 28(7) (2019) 4348.

[68] X.B. Feng, W. Fu, J.Y. Zhang, J.T. Zhao, J. Li, K. Wu, G. Liu, J. Sun, Effects of nanotwins on the mechanical properties of AlxCoCrFeNi high entropy alloy thin films. Scr. Mater., 139 (2017) 71.

[69] V. Maier-Kiener, B. Schuh, E.P. George, H. Clemens, A. Hohenwarter, Insights into the deformation behavior of the CrMnFeCoNi high-entropy alloy revealed by elevated temperature nanoindentation. J. Mater. Res., 32(14) (2017) 2658.

[70] G. Laplanche, J. Bonneville, C. Varvenne, W.A. Curtin, E.P. George, Thermal activation parameters of plastic flow reveal deformation mechanisms in the CrMnFeCoNi high-entropy alloy. Acta Mater., 143(C) (2018) 257.

[71] M. Komarasamy, N. Kumar, R.S. Mishra, P.K. Liaw, Anomalies in the deformation mechanism and kinetics of coarse-grained high entropy alloy. Mater. Sci. Eng. A, 654 (2016) 256.

[72] P.F. Yu, H. Cheng, L.J. Zhang, H. Zhang, Q. Jing, M.Z. Ma, P.K. Liaw, G. Li, R.P. Liu, Effects of high pressure torsion on microstructures and properties of an Al0.1CoCrFeNi high-entropy alloy. Mater. Sci. Eng. A, 655(C) (2016) 283.

[73] S. Gangireddy, B. Gwalani, R.S. Mishra, Grain size dependence of strain rate sensitivity in a single phase fcc high entropy alloy Al0.3CoCrFeNi. Mater. Sci. Eng. A, 736 (2018) 344.

[74] S. Gangireddy, B. Gwalani, V. Soni, R. Banerjee, R.S. Mishra, Contrasting mechanical behavior in precipitation hardenable Al.sub.XCoCrFeNi high entropy alloy microstructures: Single phase fcc vs. dual phase fcc-bcc. Mater. Sci. Eng. A, 739 (2019) 158.

[75] Q. Wei, Strain rate effects in the ultrafine grain and nanocrystalline regimes—influence on some constitutive responses. J. Mater. Sci., 42(5) (2007) 1709.

[76] H. Conrad, Grain size dependence of the plastic deformation kinetics in Cu. Mater. Sci. Eng. A, 341(1), (2003) 216.

[77] H. Conrad, Plastic deformation kinetics in nanocrystalline fcc metals based on the pile-up of dislocations. Nanotechnology, 18(32) (2007) 325701

[78] H.J. Frost, M.F. Ashby, Deformation-mechanism maps: the plasticity and creep of metals and ceramics (1st ed.). Pergamon Press. (1982).